bioRxiv preprint doi: https://doi.org/10.1101/2025.05.02.651799; this version posted August 2, 2025. The copyright holder for this preprint (which was not certified by peer review) is the author/funder. All rights reserved. No reuse allowed without permission.

Title

Mitochondrial heteroplasmy disrupts osteoclast differentiation and bone resorption by impairing respiratory complex I

Houfu Leng[1, #], Jiahao Jiang [2, #], Katja Gassner[3], Swati Midha[1,4,5,6], Raquel Justo-Méndez[3], Jianqing Zheng[1], Timothy Hall[7], Lin Luo[1,8], Suzanne D West[9], Tonia L. Vincent[1], Angus Wann[1,4], Kashyap A Patel[7], Joanna Poulton[10], Chris A. O'Callaghan[2], Ana Victoria Lechuga-Vieco[1,3,12,§] and Anna Katharina Simon[1,11,12,§]

[1-] Kennedy Institute of Rheumatology, University of Oxford, Roosevelt Drive, Oxford, OX3 7FY, UK.

[2-] Centre for Human Genetics, Nuffield Department of Medicine, Wellcome Centre for Human Genetics, University of Oxford, United Kingdom.

[3-] Institute for Research in Biomedicine (IRB Barcelona). The Barcelona Institute of Science and Technology, Baldiri Reixac, 10, 08028 Barcelona, Spain

[4-] School of Biological Sciences, University of Southampton, Southampton, Hampshire, SO17 1BJ UK

[5-] Centre for Predictive In Vitro Models, Queen Mary University of London, UK

[6-] Centre for Bioengineering, School of Engineering and Materials Science, Queen Mary University of London, UK

[7-]Department of Clinical and Biomedical Sciences, Faculty of Health and Life Sciences, University of Exeter, Exeter, UK.

[8-] CAMS Oxford Institute, Nuffield Department of Medicine, University of Oxford, Oxford, UK

[9-] NHS Highly Specialised Service for Rare Mitochondrial Disorders, Oxford Centre for Genomic Medicine, Oxford University Hospitals, Oxford, UK

[10-] Department of Women's and Reproductive Health, The Women's Centre, University of Oxford, Oxford, United Kingdom

[11-] Max-Delbrück-Center for Molecular Medicine, Berlin, Germany

[12-] Corresponding Authors

[#] Contributed equally

[§] Contributed equally

Abstract

Mitochondrial heteroplasmy, the co-existence of different mitochondrial genomes within a cell, is linked to aging and disease. Patients with heteroplasmy due to mitochondrial mutations experience multiple organ complications, particularly poor bone health and bone structure defects. However, the mechanisms involved are generally unknown, due largely to the difficulty of manipulating mtDNA in vivo. To overcome this, we leveraged a heteroplasmic mouse model and discovered that mitochondrial heteroplasmy affects a fundamental developmental process. Specifically, the differentiation of osteoclasts, which resorb bone tissue and maintain bone homeostasis. Mechanistically, there was a reduced localization of specifically respiratory complex I subunits in mitochondria in heteroplasmic mice, disrupting

bioRxiv preprint doi: https://doi.org/10.1101/2025.05.02.651799; this version posted August 2, 2025. The copyright holder for this preprint (which was not certified by peer review) is the author/funder. All rights reserved. No reuse allowed without permission.

ATP production and osteoclast differentiation. In addition, autophagic flux is exhausted, and the autophagy inducer spermidine restores mitochondrial health and rescues osteoclast activity, both in mice and in cells from patients with primary mitochondrial disease. Together, we identify the mechanisms by which mitochondrial heteroplasmy impacts osteoclastogenesis and discover spermidine as a modulator of this process, which presents a potential treatment for human heteroplasmic conditions such as mitochondrial diseases, which are largely untreatable.

Keywords: Osteoclast, mitochondrial DNA, heteroplasmy, Complex I, autophagy, spermidine

Graphical Abstract

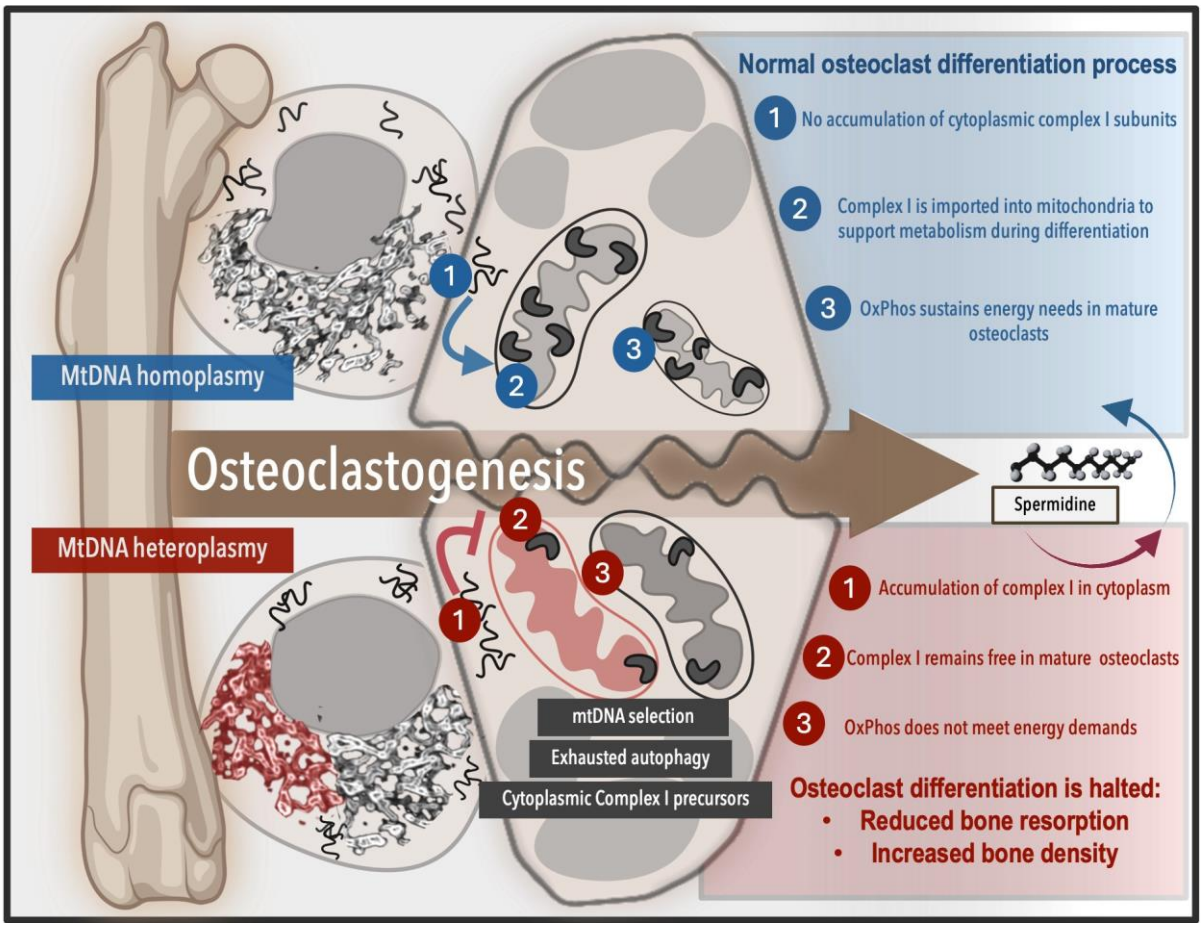

bioRxiv preprint doi: https://doi.org/10.1101/2025.05.02.651799; this version posted August 2, 2025. The copyright holder for this preprint (which was not certified by peer review) is the author/funder. All rights reserved. No reuse allowed without permission.

Main

Mitochondrial heteroplasmy, the co-existence of different mtDNA variants in one cell, can lead to a wide range of pathological phenotypes, from mild effects on cellular function to severe mitochondrial diseases. MELAS syndrome (mitochondrial encephalopathy with lactic acidosis and stroke-like episodes) is a primary mitochondrial disease caused by a pathological m.3243A>G mitochondrial point mutation in the MT-TL1 gene, which was first identified three decades ago[1,2]. Primary mitochondrial diseases, including MELAS syndrome, are also often associated with poor bone health[3] and hearing loss due to structural damage to the temporal bone[4,5]. In addition to classical mitochondrial diseases, conditions where heteroplasmy is prevalent include aging, cancer, and neurodegenerative and metabolic diseases. However, studying mitochondrial heteroplasmy in mammalian cells to identify the pathological mechanisms underlying these varied diseases is highly challenging[6] as it requires the genetic modification of mitochondrial DNA, which has not been achieved *in vivo*.

To overcome this, a heteroplasmic mouse model was developed on the C57BL/6 background, carrying a variable mixture of two mtDNA variants, C57 and NZB. NZB mtDNA differs from C57 mtDNA by several mitochondrial single nucleotide polymorphisms (SNPs), including 12 missense mutations, 4 tRNA mutations, 8 rRNA mutations, and 10 mutations in non-coding regions, making the NZB variant more efficient at oxidative phosphorylation[7]. When both variants coexist, cells selectively retain the preferred mitochondria, leading to varying degrees of heteroplasmy across different tissues and cell types[8]. This mitochondrial selection observed in mice closely reflects the mutant load distribution seen in tissues affected by primary mitochondrial diseases[9]. Importantly, heteroplasmic mice also present bone-related alterations, including elongated tibias and femurs, and early-onset kyphosis[10]. These skeletal manifestations, together with the previously described systemic metabolic dysfunction[8,10,11] , make this model compelling to dissect how mitochondrial heteroplasmy influences the fundamental developmental process of osteoclast differentiation, essential for bone homeostasis.

Bone health relies on continuous tissue remodeling via a network of bone matrix synthesizing osteoblasts (OBs) and bone resorbing osteoclasts (OCs). OCs are terminally differentiated multinucleated cells originating from myeloid progenitors in the bone marrow. The demanding environmental conditions during osteoclastogenesis require robust metabolic activity to support differentiation and function[12]. Disruptions in energy metabolism during OC differentiation cause an imbalance in skeletal homeostasis, leading to the development of bone related diseases[12]. Although the role of biogenesis of mitochondria in OC is well established[13,14,15,16,17], the contribution of other mitochondrial quality control mechanisms remains unclear. In addition to generating new mitochondria, maintaining a functional mitochondrial pool during osteoclast differentiation may also require the selective removal of damaged or less efficient organelles via mitophagy. How mitochondrial adaptation mechanisms contribute to metabolic fine tuning during osteoclast differentiation remains poorly understood, particularly in the context of mtDNA mutations. Interestingly, bone tissue

bioRxiv preprint doi: https://doi.org/10.1101/2025.05.02.651799; this version posted August 2, 2025. The copyright holder for this preprint (which was not certified by peer review) is the author/funder. All rights reserved. No reuse allowed without permission.

generally exhibits low levels of mtDNA heteroplasmy[9], suggesting that selective pressure against dysfunctional mitochondria may be particularly stringent in bone-residing cells. Whether mitochondrial selection plays an active role in ensuring successful osteoclast differentiation under heteroplasmic conditions remains unknown.

Here, we discover that mitochondrial heteroplasmy impacts osteoclastogenesis both *in vivo* and *ex vivo* using bone marrow samples from heteroplasmic mice and peripheral blood mononuclear cells (PBMCs) from m.3243A>G patients. In mice, we demonstrate that mtDNA heteroplasmy leads to increased bone density, which we attribute to defective osteoclast formation and function. Mechanistically, we identify a previously unrecognized sequential import of nuclear encoded complex I subunits into mitochondria during early differentiation of OCs, a process that is disrupted in heteroplasmic cells and leads to reduced oxidative phosphorylation and ATP production. In parallel, we reveal that mitochondrial DNA selection is essential for OC maturation, a process in which mtDNA segregation has not been previously explored. Importantly, we demonstrate for the first time that the autophagy inducing metabolite spermidine treatment restores mitochondrial quality and rescues osteoclast differentiation and function in both heteroplasmic mice and cells derived from mitochondrial disease patients. These findings offer a promising strategy for treating mitochondrial disease-associated bone pathologies.

Results

Osteoclastogenesis is impaired in heteroplasmic cells

Bone abnormalities have been reported in individuals with primary mitochondrial diseases, particularly those with heteroplasmic mitochondrial mutations[18]. To investigate whether this is caused by defective osteoclast formation, we collected blood from middle-aged individuals with MELAS carrying both healthy and m.3243A>G mutated mtDNA within their cytoplasm. This mutation has been linked previously to bone abnormalities[19]. We first verified systemic bone deficiency in our patient cohort by confirming reduced serum levels of the bone resorption marker, carboxy-terminal cross-linked telopeptide of type 1 collagen (CTX-1) (Extended Data Fig. 1a). Next, using peripheral blood mononuclear cells (PBMCs) from age- and sex-matched healthy donors and people with m.3243A>G heteroplasmy, we established an *in vitro* OC differentiation assay[20]. By day 6, mature OCs were fixed for tartrate-resistant acid phosphatase (TRAP) analysis. Using this assay, we found that the formation of mature OCs was significantly reduced in m.3243A>G cells compared to healthy cells (Fig. 1a).

As introducing mitochondrial point mutations in vivo is challenging, we used the heteroplasmic mouse model (BL/6$^{C57\text{-}NZB}$), a unique and well characterized tool in the field[8,10,21] to investigate the molecular mechanisms by which mitochondrial heteroplasmy impairs osteoclast differentiation. Bone marrow cells from BL/6$^{C57\text{-}NZB}$ heteroplasmic mice, and from BL/6^{C57} and BL/6^{NZB} homoplasmic controls, were cultured *in vitro* for 2 days with murine M-CSF to generate macrophages (day 0), followed by culture with murine M-CSF and RANKL for

bioRxiv preprint doi: https://doi.org/10.1101/2025.05.02.651799; this version posted August 2, 2025. The copyright holder for this preprint (which was not certified by peer review) is the author/funder. All rights reserved. No reuse allowed without permission.

130 5 days to induce OC formation. Consistent with our findings in human cells, bone marrow cells
131 from BL/6$^{C57\text{-}NZB}$ mice showed a significant reduction in TRAP-positive OC formation compared
132 to homoplasmic controls (Fig. 1b). These results suggest that it is heteroplasmy itself, rather
133 than complete mitochondrial and nuclear genome mismatch as in the BL/6^{NZB} cells, that
134 underlies the impaired OC differentiation observed in both the BL/6$^{C57\text{-}NZB}$ cells and patient
135 samples carrying the m.3243A>G mutation.

136 To understand the molecular mechanisms underlying this reduced osteoclastogenic capacity,
137 we conducted single-cell RNA sequencing (scRNA-seq) at various stages of OC differentiation
138 (Extended Data Fig. 1b). Bone marrow cells from the heteroplasmic and homoplasmic strains
139 were cultured for 2 days with M-CSF to generate macrophages (day 0), followed by culture
140 with M-CSF and RANKL for either 1 day or 3 days to induce OC formation. Successful *in vitro*
141 OC differentiation was validated by cross-referencing reported marker genes (e.g. *Acp5* and
142 *Ctsk* in Extended Data Fig. 1c) and negative regulators of OC following RANKL treatment (e.g.
143 *Irf8* and *Mafb*)[1] (Extended Data Fig. 1d). After applying quality control filters, we analyzed a
144 total of 10,809 cells (Extended Data Fig. 1e). Unsupervised graph-based clustering of these
145 single-cell transcriptomic profiles defined 9 distinct cell populations, including a monocyte-like
146 precursor population and a terminal OC population. Other transitional populations included
147 *Cxcl16*^{hi} macrophages, dendritic cells, early- and late-stage pre-OCs, and three proliferative
148 populations (Fig. 1c and Extended Data Fig. 1e).

149 To infer the linkage between each cell population, we computed a per-cell latent time and
150 performed partition-based graph abstraction (PAGA) analysis based on the RNA-velocity
151 dynamics[22,23](Extended Data Fig. 1f and g). These analyses revealed a cell trajectory during
152 osteoclastogenesis, which progresses from monocytic precursors to OCs, passing through
153 *Cxcl16*^{hi} macrophages, early-stage pre-OCs and late-stage pre-OCs (Extended Data Fig. 1g).
154 Notably, BL/6$^{C57\text{-}NZB}$ cells were relatively concentrated in Cxcl16^{hi} macrophages (17.4%), and
155 early-stage pre-OCs (8.0%) compared to wild-type BL/6^{C57} (14.0% and 6.5%) or BL/6^{NZB} (14.3%
156 and 6.5%) cells. Consequently, fewer heteroplasmic cells reached the mature OC population
157 (10.2% compared to 14.7% and 14.9% in BL/6^{C57} and BL/6^{NZB} cells, respectively) (Fig. 1c and
158 Extended Data Fig. 1g and h).

159 Given the high metabolic demands and finely tuned cellular adaptive mechanisms of
160 osteoclastogenesis[26], we hypothesized that mitochondrial heteroplasmy disrupts the
161 coordination of bioenergetic pathways necessary for full osteoclast maturation. To test this,
162 we performed pathway enrichment analysis, which revealed key differences in cellular
163 respiration between the genotypes, including downregulation of the tricarboxylic acid cycle
164 and of mitochondria-related functional pathways in differentiated OCs (Fig. 1d). Despite the
165 well-established hypoxic and oxidative stress environment[24,25], coupled with the high anabolic
166 demands characteristic of osteoclastogenesis[26], we found that genes involved in reactive
167 oxygen species handling were unexpectedly downregulated in BL/6$^{C57\text{-}NZB}$ cells, accompanied
168 by a shift toward catabolic metabolism (Fig. 1d).

bioRxiv preprint doi: https://doi.org/10.1101/2025.05.02.651799; this version posted August 2, 2025. The copyright holder for this preprint (which was not certified by peer review) is the author/funder. All rights reserved. No reuse allowed without permission.

169 Collectively, our findings suggest that heteroplasmic cells face challenges in osteoclastogenesis,
170 leading to premature arrest at the macrophage stage, which may be linked to altered
171 metabolic adaptation and pathway dysregulation.

172 **Alterations in complex I in heteroplasmic cells impair metabolic adaptation and oxidative**
173 **phosphorylation during OC differentiation**

174 We next analyzed the expression of genes involved in major metabolic pathways throughout
175 osteoclast differentiation in these strains. At day 0 of *in vitro* OC differentiation, there were no
176 significant differences in metabolic pathways of BL/6$^{C57\text{-}NZB}$ cells compared to wild-type BL/6^{C57};
177 only few pathways, including glycolysis, were upregulated at day 1 upon RANKL treatment in
178 BL/6$^{C57\text{-}NZB}$ cells (Fig. 2a). In contrast, after 3 days of differentiation, most mitochondrial-
179 associated pathways were downregulated in heteroplasmic OCs, including ketogenesis, Krebs
180 cycle, galactose metabolism, pentose phosphate metabolism, pyrimidine biosynthesis,
181 adenosine biosynthesis, and glutamate degradation pathway (Fig. 2a).

182 To systemically evaluate the cellular energy needs in individual cells, we aggregated the
183 expression of genes (n = 107, as annotated in the KEGG database) involved in the oxidative
184 phosphorylation (OXPHOS) pathway (Fig. 2b). As expected, OCs (cluster 2, representing the
185 most mature osteoclastic cells) displayed high OXPHOS scores than other cells along the
186 trajectory (Fig. 2b). In contrast, a significant reduction in OXPHOS score was observed in
187 BL/6$^{C57\text{-}NZB}$ OCs compared to homoplasmic controls (Fig. 2b).

188 MtDNA encodes 13 essential polypeptides that form core components of complexes I, III, IV,
189 and V[28]. We noted that all mitochondrial genome-encoded transcripts were expressed at a
190 higher level at day 3 of wild-type OC differentiation (Extended Data Fig. 2a), suggesting
191 increased energy demand in later differentiation stages. To assess the oxygen consumption
192 rate (OCR) in the OCs directly, we performed Seahorse metabolic assays. Consistent with the
193 gene expression data, no differences were observed on day 0. However, by day 1 of OC
194 differentiation, cells from BL/6$^{C57\text{-}NZB}$ mice exhibited a reduction in maximal mitochondrial
195 respiratory capacity (SRC) alongside an increase in mitochondrial mass and reactive oxygen
196 species (ROS), likely as a compensatory response (Fig. 2c and Extended Data Fig. 2b - d). These
197 results provide further evidence of compromised metabolic capacity in heteroplasmic cells
198 early in the OC differentiation process. Notably, by day 3, heteroplasmic cells exhibited lower
199 mitochondrial mass while maintaining the same spare respiratory capacity (SRC) (Extended
200 Data Fig. 2b and c), likely by utilizing alternative substrates and relying on complex II (succinate
201 dehydrogenase)[27].

202 BL/6^{C57}, BL/6^{NZB}, and BL/6$^{C57\text{-}NZB}$ cells share an identical nuclear genome but differ in their
203 mtDNA. Both mitochondrial and nuclear genomes encode subunits of the mitochondrial
204 electron transport chain (mtETC), requiring tight coordination between mitochondrial and
205 nuclear gene expression to ensure proper assembly and function. In the context of
206 heteroplasmy, where multiple mitochondrial genomes coexist, this coordination can be
207 disrupted, potentially impairing the stoichiometric assembly of the mtETC and compromising
208 oxidative phosphorylation. The reduction in bioenergetic capacity in heteroplasmic OCs was
209 further confirmed by analyzing the protein level of key mitochondrial electron transport chain

bioRxiv preprint doi: https://doi.org/10.1101/2025.05.02.651799; this version posted August 2, 2025. The copyright holder for this preprint (which was not certified by peer review) is the author/funder. All rights reserved. No reuse allowed without permission.

210 (mtETC) subunits using Western blot (Extended Data Fig 2e). BL/6$^{C57-NZB}$ cells displayed a
211 distinct expression profile, with a delayed and less pronounced increase in NDUFB8 (complex
212 I) after day 3 and only a modest rise in SDHB (complex II) levels (Extended Data Fig. 2e),
213 supporting our findings of reduced complex I representation (Fig. 2d). In contrast, wild-type
214 BL/6^{C57} cells showed a coordinated temporal upregulation of OXPHOS components. NDUFB8
215 and SDHB increased sequentially and peaked at day 3, followed by a marked rise in ATP5A
216 (complex V) at day 5. UQCR2 (complex III) and MTCOI (complex IV) also rose moderately from
217 day 3 onward. Interestingly, BL/6^{NZB} cells followed a similar pattern to BL/6^{C57}, with a sharper
218 SDHB peak and a milder ATP5A increase. While the differences between BL/6^{C57} and BL/6^{NZB}
219 may reflect mitochondrial-nuclear co-adaptation in homoplasmic cells, the divergence
220 observed in BL/6$^{C57-NZB}$ cells highlights the functional impact of mitochondrial heteroplasmy
221 on respiratory complex dynamics during differentiation. These results suggests that even if
222 some heteroplasmic cells managed to differentiate into osteoclasts, they may not have the
223 same mitochondrial metabolic performance.

224 Complexes I and II both feed electrons into the mtETC but differ in substrates and regulation,
225 making their balance essential for energy production and redox homeostasis[29]. In
226 heteroplasmic cells, this balance was altered. We observed a shift in respiratory complex
227 expression, with reduced levels of complex I (NDUFB8) relative to complex II (SDHB). These
228 differences resulted in a notable drop in the relative abundance and activation of complex I
229 compared to complex II proteins. To determine whether this imbalance translated into
230 functional consequences, we next measured complex activity and found that the altered
231 expression profile correlated with a significantly increased complex I/II activity ratio in BL/6^{C57-}
232 ^{NZB} cells specifically at day 3 (Extended Data Fig. 2f).

233 Since complexes I and II drive ATP production via the respiratory chain, we examined whether
234 heteroplasmy-related expression and activity changes affected ATP levels during osteoclast
235 differentiation. We found that BL/6$^{C57-NZB}$ cells exhibited reduced efficiency in ATP production
236 compared to wild type BL/6^{C57} OCs (Fig. 2e). This analysis examined changes in expression on
237 a per cell basis. Interestingly, when analyzed per mitochondria, heteroplasmic cells showed
238 lower levels of NDUFA9, a nuclear DNA (nDNA)-encoded subunit of respiratory complex I,
239 compared to BL/6^{C57} and BL/6^{NZB}, after day 3 of *in vitro* OC differentiation (Fig. 2f and g and
240 Extended Data Fig. 2g). In contrast, ATPβ, a subunit of Complex V (ATPase) responsible for ATP
241 synthesis, showed no difference in expression per mitochondrion in heteroplasmic cells on
242 day 3 (Fig. 2f and g). Altogether, the data suggest that dysregulation specifically of complex I
243 is the primary factor affected in OC differentiation by heteroplasmy.

244 **OC differentiation requires sequential import of complex I subunits**

245 Nuclear-encoded mitochondrial proteins are synthesized by cytosolic ribosomes as precursors
246 and need to be imported into mitochondria[30]. Among them, the complex I subunit NDUFA9
247 harbors an N-terminal cleavable pre-sequence that facilitates its mitochondrial targeting[31].
248 We used confocal imaging to track the localization of the complex I subunit NDUFA9 during
249 osteoclast differentiation. Since this had not been previously examined in wild-type cells, our

bioRxiv preprint doi: https://doi.org/10.1101/2025.05.02.651799; this version posted August 2, 2025. The copyright holder for this preprint (which was not certified by peer review) is the author/funder. All rights reserved. No reuse allowed without permission.

250 initial aim was to characterize the sequential import dynamics under physiological conditions.
251 In BL/6^{C57} cells, a distinctive feature of early differentiation was the prominent cytoplasmic
252 presence of NDUFA9 (Fig. 2g and Extended Data Fig. 2g), which progressively shifted to a
253 mitochondrial localization (identified by TOM20 staining) by day 5, indicating efficient import
254 during normal osteoclastogenesis (Fig. 3a, b).

255 Previous studies indicate that complex I alterations disrupts mitochondrial protein import,
256 impairs chaperone function, and activates the mitochondrial unfolded protein response to
257 prevent aggregation of respiratory complex subunits[32]. Consistent with this, we found that
258 the progressive mitochondrial import of NDUFA9 observed in wild-type BL/6^{C57} cells was
259 notably reduced in BL/6^{NZB} cells, and even more markedly in BL/6$^{C57\text{-}NZB}$ cells. By day 5,
260 mitochondrial colocalization of NDUFA9 was significantly diminished in both genotypes,
261 suggesting impaired import or retention of this subunit under conditions of heteroplasmy and
262 mitonuclear mismatch (Fig. 3a, b). This suggests that the reduced import of nuclear-encoded
263 complex I subunits arises from impaired mitochondrial import machinery, likely triggered by
264 nucleo-mitochondrial imbalance or stress responses. Supporting this, scRNA-seq revealed
265 reduced nuclear-encoded complex I subunits and increased mitochondrial-encoded genes in
266 heteroplasmic OCs (Fig. 2d), consistent with a stress response that may impair import and
267 complex I assembly.

268 To directly address this, we analyzed scRNA-seq data for gene expression changes related to
269 mitochondrial protein import and the mitochondrial degradome at days 0, 1, and 3 of OC
270 differentiation. We found pronounced downregulation of genes encoding key components of
271 the mitochondrial protein import machinery in BL/6$^{C57\text{-}NZB}$ cells compared to wild type BL/6^{C57}
272 cells (Fig. 3c). Genes involved in mitochondrial protein degradation were also reduced in
273 heteroplasmic cells (Fig. 3d), potentially contributing to the cytoplasmic accumulation of
274 complex I subunits. Furthermore, our data indicates a downregulation of the assembly
275 proteins for respiratory complex I (Fig 3e), suggesting that the failure to complete protein
276 import into mitochondria leads to decreased respiratory complex assembly factors in BL/6$^{C57\text{-}}$
277 ^{NZB} cells compared to BL/6^{C57}.
278 Altogether, our data suggest that nuclear-encoded complex I subunits fail to be either
279 imported into mitochondria or properly degraded in the cytoplasm during OC differentiation
280 in BL/6$^{C57\text{-}NZB}$. Both processes require ATP[30,33,34], which is reduced with heteroplasmy at the
281 stage when OCs would normally depend on respiratory complex I formation for mitochondrial
282 function.

283 **Mitochondrial selection in heteroplasmic cells is essential for osteoclast differentiation**

284 We previously reported that mitochondrial heteroplasmy can be resolved through non-
285 random mtDNA selection, a process that is tissue- and cell-type specific[8]. Given the substantial
286 metabolic shifts that occur during osteoclastogenesis[35], we hypothesized that different stages
287 of OC differentiation impose distinct bioenergetic demands, potentially requiring active
288 mitochondrial selection.

bioRxiv preprint doi: https://doi.org/10.1101/2025.05.02.651799; this version posted August 2, 2025. The copyright holder for this preprint (which was not certified by peer review) is the author/funder. All rights reserved. No reuse allowed without permission.

To evaluate mtDNA proportion changes during differentiation, we adapted the mgatk pipeline to genotype mitochondrial variants at single-cell resolution using deep scRNA-seq libraries during early OC differentiation[36]. After strict filtering, we were able to recover on average 237 reads per cell covering the NZB mtDNA haplotype (Extended Data Fig. 3a). We observed a higher level of NZB mtDNA transcripts on day 3 compared to day 1 cells, independent of the sequencing depth (Fig. 4a). The percentage of NZB mtDNA also slightly increased along the OC differentiation trajectory (Extended Data Fig. 3b). We further validated these findings using PCR followed by RFLP (Restriction Fragment Length Polymorphism) analysis[21,37,38] in OC cultures at Days 1 and 3. Our data showed a shift toward more NZB mtDNA as OC differentiation progresses (Fig. 4b and Extended Data Fig. 3c, d). This change in mtDNA proportion from day 1 to day 3 was driven by the formation of mature OCs, which carried increased NZB mtDNA content (Fig. 4c). Other cells did not show significant enrichment for the NZB mtDNA haplotype compared to monocytic precursors (Fig. 4c). These results suggest that the selection of the preferred mtDNA variant, reflected in the higher proportion of NZB mtDNA in mature OCs, facilitates OC maturation. Moreover, the selection towards a mtDNA haplotype different from the nuclear genome suggests that the pathogenic phenotypes observed in heteroplasmic OCs were indeed caused by heteroplasmy per se, rather than specific SNPs from the NZB mitochondrial genome.

While failed mitochondrial selection has previously been associated with impaired autophagy[10], it remains unclear whether mitophagy clears unwanted mitochondria in mtDNA heteroplasmic osteoclasts. On day 1, BafA1 treatment increased LC3-II levels and decreased the LC3-I/LC3-II ratio, indicating a strong autophagic flux across all genotypes (Fig. 4d, e). However, by day 3, BafA1, which was used to block autophagosome-lysosome fusion and assess autophagy flux, no longer increased LC3-II in BL/6$^{C57\text{-}NZB}$ cells (Fig. 4d, e). This, together with elevated p62 levels in heteroplasmic cells, even in the absence of BafA1 (Fig. 4d and Extended Data Fig. 3e), suggests a block in autophagic flux at day 3. Together, these results suggest that reduced autophagy throughout differentiation may underlie the metabolic alterations observed in heteroplasmic OCs.

Osteoclast maturation in murine and human heteroplasmic cells can be restored by promoting mtDNA selection through spermidine supplementation

We previously demonstrated that autophagy is regulated by endogenous spermidine levels which control translation of TFEB[39,40]. Spermidine also activates mitochondrial translation in myeloid cells[41] and boosts oxidative metabolism by binding to the mitochondrial trifunctional protein (MTP) in T cells[42]. Spermidine given to mice in the drinking water restores autophagy levels when these are low[43]. Therefore, we used spermidine to directly test whether it improves mitochondrial function and resolves the altered metabolic phenotype observed in heteroplasmic OCs. First, we performed OC differentiation of cells from heteroplasmic mice with spermidine supplementation in the culture media. Spermidine restored OC formation in heteroplasmic cells *in vitro* compared to control cultures (Fig. 5a, b). Interestingly, the spermidine dose required to rescue OC differentiation in heteroplasmic cells has previously

bioRxiv preprint doi: https://doi.org/10.1101/2025.05.02.651799; this version posted August 2, 2025. The copyright holder for this preprint (which was not certified by peer review) is the author/funder. All rights reserved. No reuse allowed without permission.

329 been shown to inhibit osteoclast formation in wild-type cells[44] - a result we also confirmed in
330 our analyses (Fig. 5a, b). This suggests that heteroplasmic cells have exhausted their
331 endogenous spermidine levels and now have a higher demand for spermidine to support
332 proper differentiation. Spermidine supplementation significantly increased NZB mtDNA
333 selection on day 5 (Fig. 5c), while the total mtDNA content remained stable (Extended Data
334 Fig. 4a).

335 While no changes in total ATP were observed in the spermidine-treated OC cultures on day 1
336 of differentiation (Extended Data Fig. 4b), treated heteroplasmic cells showed a sharp increase
337 in ATP content on day 3 (Fig. 5d). Interestingly, despite this increase, ATPβ levels were reduced
338 in BL/6^{C57}, BL/6^{NZB} and BL/6$^{C57\text{-}NZB}$ cells by day 5 (Extended Data Fig. 4c, d). Confocal imaging
339 revealed increased mitochondrial complex I expression relative to mitochondrial content
340 specifically in spermidine-treated OC cultures from BL/6$^{C57\text{-}NZB}$ mice on day 5, with no similar
341 effect observed in the other genotypes (Fig. 5e and Extended Data Fig. 4d). These findings
342 suggest that spermidine treatment improves mitochondrial efficiency and promotes ATP
343 synthesis by boosting complex I function and mitochondrial respiratory capacity, rather than
344 simply increasing ATP synthase levels.

345 To extend the relevance of our findings to a human context, we tested whether spermidine
346 could improve osteoclast differentiation in cells derived from individuals carrying the
347 m.3243A>G mitochondrial mutation. While spermidine has been previously linked to
348 autophagy and mitochondrial maintenance, its effects have not been evaluated in the setting
349 of mitochondrial heteroplasmy in primary human cells. Treatment with 10 µM spermidine
350 increased both the number of TRAP^{+} OCs (Fig. 5f) and intracellular ATP levels (Fig. 5g) in
351 m.3243A>G cells, supporting its potential to enhance mitochondrial function and restore
352 differentiation capacity in this pathogenic context.

353 Together, these results position spermidine as a promising metabolite supplement capable of
354 improving the phenotype of cells that require mitochondrial heteroplasmy resolution for
355 proper differentiation and function.

356 **BL/6$^{C57\text{-}NZB}$ mice exhibit increased bone density due to diminished OC function**

357 Next, we assessed how mitochondrial heterogeneity in OCs and their impaired differentiation
358 affects bone homeostasis in vivo. Unlike in humans, the heteroplasmic mouse model lacks
359 nuclear genetic variation between individuals, allowing us to specifically study the effects of
360 mitochondrial differences without genetic confounders, providing a controlled setting to
361 investigate this phenomenon *in vivo*. We first investigated whether bone-resorbing OCs are
362 affected in BL/6$^{C57\text{-}NZB}$ mice by staining longitudinal cross-sections of tibiae with TRAP specific
363 for OC. According to bone histomorphometry, tibiae from BL/6$^{C57\text{-}NZB}$ mice had significantly
364 lower signal for TRAP-positive OC when compared to those from BL/6^{C57} control mice (Fig. 6a,
365 b). Consistently, a significant reduction of CTX-1 level was observed in serum from BL/6$^{C57\text{-}NZB}$
366 mice, indicating a lower level of systemic OC activity and bone resorption (Fig. 6c). No
367 differences were observed in the frequency of bone marrow OC precursors as demonstrated
368 by expression of surface markers (CD11b^{-}CD3^{-}B220^{-}CD115^{+}) between the 3 genotypes,

bioRxiv preprint doi: https://doi.org/10.1101/2025.05.02.651799; this version posted August 2, 2025. The copyright holder for this preprint (which was not certified by peer review) is the author/funder. All rights reserved. No reuse allowed without permission.

369 indicating specifically a diminished OC differentiation from BL/6$^{C57\text{-}NZB}$ OC precursors (Extended
370 Data Fig. 5a). In addition, no differences were observed in serum procollagen type I N-terminal
371 propeptide (PINP), an OB-derived marker reflecting bone formation, among the three groups
372 (Fig. 6d).

373 To investigate if bone mass is affected in BL/6$^{C57\text{-}NZB}$ mice, tibiae were collected from aged-
374 matched male BL/6^{C57}, BL/6^{NZB} and BL/6$^{C57\text{-}NZB}$ mice for micro-CT analysis. BL/6$^{C57\text{-}NZB}$ mice
375 showed an increase in trabecular bone (Fig. 6e). Accordingly, quantification of bone
376 parameters revealed a 1.3-fold increase of bone volume over total volume (BV/TV) and a 1.2-
377 fold increase of trabecular thickness (Tb.Th), accompanied by a significant decrease in bone
378 surface over bone volume (BS/BV) and in trabecular separation (Tb.Sp) (Fig. 6f). The decrease
379 in the BS/BV ratio in BL/6$^{C57\text{-}NZB}$ group was due to a significant increase in BV, as compared to
380 BS. Furthermore, a significant increase of cortical thickness (Ct.Th) and cortical area (Ct.Ar) was
381 observed in the BL/6$^{C57\text{-}NZB}$ group (Fig. 6g), confirming amelioration of overall bone parameters.
382 Next, we investigated whether these changed bone parameters affected bone strength by
383 measuring resistance to fracture. We conducted biomechanical compression testing of the
384 femur from BL/6^{C57} mice, BL/6^{NZB} mice and BL/6$^{C57\text{-}NZB}$ mice (Fig. 6h). Compared with femurs
385 from BL/6^{C57} mice, those from BL/6$^{C57\text{-}NZB}$ mice needed 25% more maximum load to break (Fig.
386 6i). Therefore, the femur from BL/6$^{C57\text{-}NZB}$ had increased bone mechanical strength, resulting
387 in greater resistance to deformation or fracture.

388 Our results showing impaired OC differentiation, along with serum CTX-1 and PINP analyses,
389 indicate that the bone alterations observed in BL/6$^{C57\text{-}NZB}$ mice are likely driven by diminished
390 OC activity, rather than changes in other non-hematopoietic cells such as OBs. To test this, we
391 performed bone marrow (BM) chimera experiments, where the host provides the OBs and the
392 donor supplies the OCs, given their hematopoietic origin (Fig. 6j, k and Extended Data Fig. 5b-
393 d). Lethally irradiated BL/6$^{C57\text{-}NZB}$ and BL/6^{C57} mice were transplanted with BM donor cells from
394 either BL/6^{C57} or BL/6$^{C57\text{-}NZB}$ mice. BM engraftments were monitored by bleeding every 2
395 weeks, with the donor cells expressing the CD45.2 isoform while the host was CD45.1^{+} to track
396 donor and host cells (Extended Data Fig. 5b-c). Notably, we observed an overall increase in
397 bone density, as indicated by BV/TV measurements, when the BM was heteroplasmic (Fig. 6j,
398 k), along with changes in additional parameters assessed by micro-CT analysis (Extended Data
399 Fig. 5d), regardless of the recipient strain. These findings indicate that the increased bone
400 volume in BL/6$^{C57\text{-}NZB}$ mice is driven by impaired differentiation and formation specifically of
401 OCs, which are of hematopoietic origin.

402 Building on our *in vitro* findings that spermidine restores OC differentiation in heteroplasmic
403 cells, we next investigated whether spermidine could also modulate this phenotype *in vivo*
404 (Fig. 6l-n and Extended Data Fig. 5e). We generated BM chimeric mice by transplanting BM
405 donor cells from wild-type BL/6^{C57} or BL/6^{C57NZB} mice into lethally irradiated BL/6$^{C57\text{-}NZB}$
406 recipients, ensuring that all recipient mice share the same host tissue background. After 8
407 weeks of spermidine treatment (5 mM in drinking water), bone phenotyping analyses using
408 micro-CT demonstrated that spermidine administration in BL/6$^{C57\text{-}NZB}$ BM donor cells led to a
409 decrease of BV/TV in mice (Fig. 6m), accompanied by an increase in Tb. Sp (Extended Data Fig.

bioRxiv preprint doi: https://doi.org/10.1101/2025.05.02.651799; this version posted August 2, 2025. The copyright holder for this preprint (which was not certified by peer review) is the author/funder. All rights reserved. No reuse allowed without permission.

5e), confirming an activation of bone catabolism. Lastly, spermidine-treated chimeric BL/6$^{C57-NZB}$ mice showed decreased bone mechanical strength, reversing the phenotype to resemble wild-type BM (Fig. 6n).

Taken together, OC differentiation in heteroplasmic cells is linked to a shift in mitochondrial heteroplasmy toward NZB mtDNA variants. By restoring spermidine levels that may have been depleted due to the extra demand during heteroplasmic cell differentiation, osteoclastogenesis was restored, both *in vitro* and *in vivo.*

Discussion

Mitochondrial heteroplasmy can arise in healthy individuals through the random accumulation of mitochondrial DNA mutations and underlies the symptoms of mitochondrial diseases caused by pathogenic variants. These disorders often affect multiple organs, though the reasons for tissue-specific vulnerability remain unclear. In this study, we demonstrate that mitochondrial heteroplasmy impairs the highly energy-demanding process of osteoclast differentiation, specifically at the stage when mitochondrial respiration becomes essential. Importantly, we could uncover for the first time that when nuclear encoded complex I of the mtETC does not match the mitochondrial encoded mtETC components, its import into the mitochondria and thereby the proper assembly of the mtETC is impaired, affecting ATP metabolism. Heteroplasmy leads to premature termination of osteoclastogenesis and thereby reduced bone resorption. We further demonstrate that autophagic flux gets exhausted over the course of heteroplasmic OC differentiation and spermidine, a metabolite needed for autophagy, partially rescues OC function in both heteroplasmic mice and in heteroplasmic patients' cells.

The generation of new mitochondrial DNA (mtDNA) and proteins has been linked to OC differentiation and function. Indeed, mature OCs have bigger and larger numbers of mitochondria, elevated mitochondrial oxygen consumption rates and higher levels of the mtETC enzymes[13,17]. Notably, RANKL has been shown to stimulate mitochondrial biogenesis[17,45]. The extensive transcriptional and metabolic reprogramming and intact mitochondrial function are essential for OC differentiation and to demineralize the bone.

The assembly of mitochondrial respiratory complex I in mammals requires the coordinated integration of at least 44 subunits encoded by either nuclear or mitochondrial genomes[46]. The presence of complex I subcomplexes (intermediate state) in complex I-deficient cells (i.e. when the complex is not assembled properly) indicates a sequential assembly process[47,48,31]. This involves the complete import of nuclear-encoded subunits into mitochondria, degradation of excess cytoplasmic material, and ultimately, the proper assembly and superassembly of respiratory complex I in the mitochondrial lumen. Although not all mtDNA mutations directly affect mtETC subunits, such as the m.3243A>G MELAS mutation in a mitochondrial tRNA gene, they can still disrupt mitochondrial protein synthesis or quality control, which in turn can impair mtETC subunit expression and function. Our data suggests that mitochondrial protein subunits, in particular complex I, accumulate as unimported mitochondrial proteins in the

bioRxiv preprint doi: https://doi.org/10.1101/2025.05.02.651799; this version posted August 2, 2025. The copyright holder for this preprint (which was not certified by peer review) is the author/funder. All rights reserved. No reuse allowed without permission.

450 cytoplasm during OC differentiation. The absence of Ndufs4, a subunit of complex I in the
451 mtETC encoded by the nuclear genome, has been associated with impaired OC differentiation
452 and function, leading to increased bone density[49]. In addition, it has been reported that ECSIT,
453 a complex I-associated protein, plays a central role in the mitochondrial response to early
454 signaling of RANKL[45]. Osteoclastogenesis is a tightly regulated process that demands ATP not
455 only for biomass generation but also for metabolic adaptation to substrate availability at
456 different stages. This process unfolds in a hypoxic tissue environment[25,50]. Intriguingly,
457 hypoxia-induced mitochondrial stress granules have been identified in C. elegans[51]. Similarly,
458 during aerobic growth, yeast cells were shown to accumulate mitochondrial precursor
459 proteins as MitoStores in the cytoplasm[52]. Hence, one explanation for complex I being
460 retained in the cytoplasm may be that this temporary storage site ensures their rapid import
461 into mitochondria during the later stages of differentiation, particularly under challenging
462 nutritional conditions or hypoxic induction. However, unassembled complex I accumulate in
463 the cytoplasm and are bound for degradation. Previous studies in mammalian cells suggest
464 that stress granules can be cleared either through an autophagy-independent disassembly
465 process or via autophagy-dependent degradation[53,54]. The impaired autophagic flux observed
466 in the latter stages during OC differentiation in heteroplasmic BL/6$^{C57\text{-}NZB}$ cells may contribute
467 to the cytoplasmic accumulation of complex I.
468 Mitochondrial heteroplasmy presents a largely unexplored area that may influence cellular
469 function and bone health. Spermidine has been proposed to enhance autophagy[40,55],
470 translational activity[43] and mitochondrial metabolism[42,56,57]. Collectively, these findings
471 highlight spermidine as a promising candidate for improving mitochondrial quality. We and
472 others have found that in both mice and humans a moiety of spermidine is needed to activate
473 the translation factor *eif5a* by hypusination in order to increase autophagic flux and lysosomal
474 activity[43,58]. Additionally, this translation factor is crucial for mitochondrial translation[41], and
475 in T cells boosts oxidative metabolism by binding to the mitochondrial trifunctional protein
476 (MTP)[42]. This implies that cellular spermidine levels may run low if this pathway is repeatedly
477 triggered such as in heteroplasmy. Spermidine may need to be replenished or else an
478 'exhausted type' of autophagic flux occurs where LC3- II is no longer degraded, as we found
479 here. We also observed that in wild-type cells spermidine inhibits OC differentiation. This is in
480 line with a study that showed supplementation with spermine or spermidine enhances bone
481 strength by inhibiting OCs, whereas inhibiting polyamine biosynthesis reduces these benefits[44].
482 The differentiation of OC, like that of most cell types, requires autophagy and spermidine may
483 help under homeostatic conditions. In contrast, in heteroplasmic mice, we found that
484 spermidine enhanced OC differentiation at the dose that was previously reported to inhibit
485 the process in wild-type cells[44]. Similar results have been observed in Nrf2 knockout cells[59],
486 suggesting that spermidine levels may be critically low and need to be replenished under
487 certain stressful situations such as excessive ROS, or repeated clearance of either
488 mitochondria or unwanted complexes I in the cytoplasm.

489 Our findings demonstrate that spermidine treatment can restore the assembly process and
490 protein import leading to improved mitochondrial function in human *in vitro* OC

bioRxiv preprint doi: https://doi.org/10.1101/2025.05.02.651799; this version posted August 2, 2025. The copyright holder for this preprint (which was not certified by peer review) is the author/funder. All rights reserved. No reuse allowed without permission.

differentiation, as well as *in vivo* in mice. The m.3243A>G mutation in MELAS patients, which affects a mitochondrial tRNA gene, and the heteroplasmic BL/6$^{C57\text{-}NZB}$ mice both exhibit mitochondrial genetic variability, making them comparable models for studying the effects of heteroplasmy. However, it is unclear why the m.3243A>G mutation is pathogenic and why some individuals carrying it are asymptomatic. The human mitochondrial genome is under heavy evolutionary constraint to adapt to the nuclear genome , even without pathogenic mutations[60,61]. A certain threshold of mtDNA mutational load may need to be reached before nucleo-mitochondrial incompatibility arises and MELAS symptoms develop. However, prior work in both mice[8] and humans[60] suggests that selection does not always favor nuclear-matching mtDNA variants, indicating forces beyond mitonuclear mismatch. It remains unclear to what extent mitochondrial diseases such as MELAS arise from the accumulation of pathogenic variants leading to mitonuclear mismatch, versus being driven by heteroplasmy itself. Since one of the mouse models in our work features complete mitonuclear mismatch (BL/6^{NZB}), we have effectively isolated the influence of heteroplasmy, a distinction that is difficult to achieve in human in vivo samples.

Comparing these murine and human models of disease allowed us to identify shared mechanisms underlying mitochondria-related abnormalities of osteoclastogenesis and led to the discovery of spermidine as a modulator of this process. This finding opens the door for the potential use of spermidine in human heteroplasmic conditions, such as mitochondrial diseases, a therapeutic possibility not previously reported.

Materials and methods

Lead Contact and Materials Availability

Further information and requests for resources and reagents should be directed to and will be fulfilled by the Lead Contacts, Anna Katharina Simon (katja.simon@kennedy.ox.ac.uk) and Ana Victoria Lechuga-Vieco (ana.lechugavieco@irbbarcelona.org).

Materials availability

Animal lines generated in this study will be made available on request, but we may require a payment and/or a completed Materials Transfer Agreement if there is potential for commercial application.

Data and code availability

All data reported in this paper will be shared by the lead contact upon request. Original sequencing data files have been deposited at NCBI-SRA (PRJNA1144799), with a temporary link to access the metadata: (https://dataview.ncbi.nlm.nih.gov/object/PRJNA1144799?reviewer=45rhoehhhq1rkj66o92nrv2pds). Links or accession numbers are also listed in the key resources table. The datasets will be publicly available upon the publication of this manuscript. This paper does report original

bioRxiv preprint doi: https://doi.org/10.1101/2025.05.02.651799; this version posted August 2, 2025. The copyright holder for this preprint (which was not certified by peer review) is the author/funder. All rights reserved. No reuse allowed without permission.

code. The code for 3D bone shape reconstruction/evaluation and OC/OB quantification for in-vitro staining (Supplementary Table 2) can be found in GitHub repository: https://github.com/jianqingzheng/image_processing. Any additional information required to reanalyze the data presented in this work is available from the from the Lead Contact upon request.

Experimental model and subject details

Animals

All animal experiments were done in compliance with the guidelines established by the UK Animal (Scientific Procedures) Act 1986 and the Institutional Animal Care and Use Committee of the Barcelona Science Park and University of Barcelona. In vivo experiments with animals were undertaken under the UK Home Office Project License PPL 30/3388. Unless otherwise specified, all experiments were performed in 8- to 12-week-old mice in a C57BL/6JOlaHsd background and a heteroplasmic mouse strain with the nuclear genome of C57BL/6JOlaHsd but mitochondrial DNA of C57+NZB (referred to as BL/6$^{C57\text{-}NZB}$)[10]. Mice were housed in specific pathogen-free facilities at the Kennedy Institute of Rheumatology (NDORMS, University of Oxford) and Park Scientific of Barcelona (PCB) under a 12-hour light/dark cycle and had ad libitum access to water and a standard chow diet (SDS diets 801,151; 75% energy from carbohydrates, 17.5% from protein, and 7.5% from fat).

Patient samples

Patient blood samples were obtained with the approval of the United Kingdom National Research Ethics Service (South Central-Berkshire, approval number 20/04, IRAS 162181). Written informed consent was obtained from all participants, and all procedures were carried out in accordance with relevant national and international guidelines and regulations. This research has been conducted using the UK Biobank Resource. This work was carried out under UK Biobank project number 103356.

Methods details

Micro computed tomography (µCT) scan and analysis of bone structure

The PerkinElmer QuantumFX scanner was utilized to scan the tibiae. The region of interest was specified as 100 slices below the growth plate of the proximal tibia and scanned for 3 minutes with an energy of 90KV, 200uA, and field of view of 10. The resulting bone data from the scan were subjected to analysis using Analyse-12.0 software and Analyse-14.0 software.

Compression testing of femur

After being harvested, the femurs were stored directly in -20 °C. To prepare for the compression test, the femurs were rehydrated with PBS at 4 °C overnight. Murine right femora were subjected to compression test using Electroforce 5500 (TA Instruments, Germany) on a 200 N load. Bones were secured on the lower plate and compressed. For testing, the bones were pre-loaded with a contact force of -0.5 N and load-displacement curves were generated

bioRxiv preprint doi: https://doi.org/10.1101/2025.05.02.651799; this version posted August 2, 2025. The copyright holder for this preprint (which was not certified by peer review) is the author/funder. All rights reserved. No reuse allowed without permission.

565 in displacement control at a cross-head speed of 0.3 mm/s until failure of the diaphyseal region.
566 Ultimate load was recorded for each group as an indicator of bone strength.

567 Serum and BM tissue processing

568 On the day of sacrifice, intracardiac puncture was used to collect mouse blood samples using
569 capillary blood collection tubes (16.440, Microvette® CB 300 Z). The collected blood samples
570 were kept on ice for up to 2 hours and then centrifuged at full speed for 5 minutes to extract
571 the serum (supernatant). Serum was stored at −80 °C until further analysis. To collect mouse
572 BM cells, the femurs were crushed with a mortar and pestle in PBS-0.1% BSA-2 mM EDTA. The
573 mixture was then filtered through 70 µm cell strainers, and the collected cells were stored on
574 ice, ready for flow cytometry without RBC lysis.

575 ELISA (Enzyme-Linked Immunosorbent Assay)

576 Mouse serum CTX1 level, mouse serum P1NP level and human serum CTX1 level were
577 measured by ELISA according to the manufacturer's instructions.

578 Tartrate-Resistant Acid Phosphatase (TRAP) Staining

579 TRAP staining and counterstained with 0.2% methyl green solution experiments were
580 previously described[20] and conducted according to the manufacturer's instructions. TRAP
581 positive multi-nuclear (>3 nuclei) OC were counted. The Zeiss AxioScan Z1 Slide Scanner at the
582 Wolfson Imaging Centre, WIMM, University of Oxford was used to acquire the images of OC.

583 TRAP staining and histomorphometry analysis of tibiae

584 Tibiae were fixed in 4% PFA at 4 °C overnight and then decalcified in 10%
585 Ethylenediaminetetraacetic acid (EDTA) decalcification solution for a duration of 14 days
586 (buffer changed every 3 days). After decalcification, the tibiae were paraffin embedded for
587 sectioning using a Leica RM2235 microtome, resulting in sections of 5 µm thickness to create
588 histology slides (VWR 631-1553). The sections were processed and stained with TRAP solution,
589 followed by counterstaining with 0.2% methyl green solution. Histology slides were scanned
590 using the Hamamatsu NanoZoomer S210 (WIMM, the University of Oxford). OC parameters
591 from histology slides were manually quantified by a researcher from JingLianWen Technology
592 (https://www.jinglianwen.com) blinded to the mouse experiment groups.

593 Bone Marrow Transplant and chimera blood lineages analysis

594 To establish BM chimeras, 8-12-week-old female BL/6$^{C57\text{-}NZB}$ mice and CD45.1^{+} B6.SJL female
595 mice were lethally irradiated at the dose of 11 Gy (550 cGy twice, 4 hours apart) and rested
596 for 1 hour prior to injection. 1.5 million BM cells derived from 8-12-week-old BL/6$^{C57\text{-}NZB}$ and
597 BL/6^{C57} female mice or their respective littermates were transplanted (i.v. injection) into these
598 irradiated mice. Reconstitution effectiveness was evaluated by analysing the percentage of
599 CD45.1^{+}, CD45.2^{+} and CD45.1/2^{+} cells in the blood PBMCs of bone marrow-transplanted mice
600 at 2,4, 6- and 8-weeks post-irradiation. To achieve this, we collected 50 microliters of blood
601 from tail vein bleeding and treated it with RBC Lysis Buffer for 5 minutes. After centrifugation,

bioRxiv preprint doi: https://doi.org/10.1101/2025.05.02.651799; this version posted August 2, 2025. The copyright holder for this preprint (which was not certified by peer review) is the author/funder. All rights reserved. No reuse allowed without permission.

602 the supernatant was removed, and the cells were stained with antibodies for flow cytometry
603 analysis. Given that previous research[62] demonstrated that three weeks is sufficient for OC
604 replenishment after transplantation, mice were sacrificed 8-9 weeks following lethal
605 irradiation and transplantation.

606 This ensured comprehensive reconstitution of most cell lineages with the transplanted cells.
607 Both blood and bone samples were collected for further analysis.

608 Mouse In vitro OC differentiation

609 Mouse in vitro OC differentiation method was previously described[20]. In brief, 8-week-old
610 mouse BM cells were treated with 50 ng/ml M-CSF in Alpha-MEM culture media with 10% FBS,
611 1% pen/strep, and 1% L-glutamine for 48 hours (day -2) in 96-well plates. On day 0, the
612 adherent cells were differentiated into OCs with 10 ng/ml mouse M-CSF and 50 ng/ml mouse
613 RANKL. Spermidine was added at the dosage of 10µM. Culture media was refreshed every 3
614 days and OCs were identified by TRAP staining on day 5. The Olympus BX51 microscope at the
615 Kennedy Institute of Rheumatology and AID ELISpot Reader System (ELR078IFL, AID GmbH) at
616 the Wellcome Centre for Human Genetics were used to acquire the images of OC.

617 Flow Cytometry

618 Bone marrow and blood samples were collected from mice and prepared for flow cytometry.
619 Erythrocytes were lysed using eBioscience™ 1x RBC Lysis Buffer. Cells were first incubated with
620 FcR blocker in PBS for 20 minutes, followed by incubation with surface-conjugated antibodies
621 for 30 minutes at 4°C. Conjugated antibodies used for surface staining were: anti-CD45.1, anti-
622 CD45.2, anti- CD45R, anti-CD3e, anti-CD11b, anti-CD117 and anti-CD115. Identification of
623 viable cells was done by fixable Zombie Aqua Live/Dead or near-IR dead cell staining. Stained
624 samples were fixed with BD Cytofix™ Fixation Buffer for 15 minutes at RT. All samples were
625 washed and stored in PBS containing 5 mM EDTA (Sigma-Aldrich) and 2% FBS (Sigma-Aldrich)
626 before acquisition. To determine the absolute cell count within tissues, 10,000 or 20,000
627 CountBright™ absolute counting beads were added to each sample before flow cytometry to
628 determine the total cell count per bone or blood volume. To ensure accuracy, over 2,000 beads
629 were acquired per tube. Samples were acquired on a FACS LSR II (R/B/V) or Fortessa X20
630 (R/B/V/YG) flow cytometer (BD Biosciences) using FACSDiva software and analysed with
631 FlowJo (version 10.10, BD Biosciences).

632 *Mitochondrial content and ROS levels during OC differentiation:* Mitochondrial content and
633 ROS levels were assessed using Nonyl acridine orange (NAO) and CellROX™ Deep Red dyes.
634 Cells were collected and incubated with 100 nM NAO and 5 µM CellROX™ for 20 minutes at
635 37°C. Ex/Em: 450/530 nm for NAO and 644/665 nm for CellROX™. After washing, cells were
636 surface-stained and prepared for flow cytometry analysis as described in the previous section.

637 *Autophagy flux (Flow cytometry).* Autophagy levels were assessed as previously described[39].
638 In brief, cells were treated for 2 hours with either bafilomycin A1 (10 nM BafA1) or vehicle
639 control, followed by staining using the FlowCellect™ Autophagy LC3 Antibody-based assay kit.

bioRxiv preprint doi: https://doi.org/10.1101/2025.05.02.651799; this version posted August 2, 2025. The copyright holder for this preprint (which was not certified by peer review) is the author/funder. All rights reserved. No reuse allowed without permission.

640 After labeling with surface markers (as described earlier), cells were washed with Assay Buffer
641 in 96-well U-bottom plates. Permeabilization was performed with 0.05% saponin, followed by
642 immediate centrifugation. Cells were then incubated with anti-LC3 (FITC) at 1:20 dilution in
643 Assay Buffer for 30 minutes at 4°C, followed by a final wash with 150 µL Assay Buffer.
644 Autophagic flux was determined by calculating the LC3-II median fluorescence intensity as
645 (BafA1 - Vehicle) / Vehicle.

646 Pre-processing of single-cell RNA-seq data

647 To collect mouse BM cells, the femurs were crushed with a mortar and pestle in PBS-0.1% BSA-
648 2 mM EDTA. The mixture was then filtered through 70 µm cell strainers, and the collected cells
649 were plated for in vitro OC differentiation with 50 ng/ml M-CSF in Alpha-MEM culture media.
650 On day 0, the adherent cells were differentiated into OCs with 10 ng/ml mouse M-CSF and 50
651 ng/ml mouse RANKL. Cells were harvested at the specified time points and were labeled with
652 Cell Multiplexing Oligos (10x Genomics) according to the manufacturer's instructions.
653 Barcoded sequencing libraries of multiplexed single-cell samples were generated using 10X
654 Genomics Chromium system with 3' chemistry. Due to a technique issue, two of the three
655 biological replicates were pooled together prior to the multiplexing step and were treated as
656 single replicate (rep2) in the downstream analysis.

657 Computational analysis of single-cell RNA-seq data

658 Raw gene counts were normalized by sequencing depth and log1p transformed in Seurat.
659 Batch effects were corrected using harmony[63] with n=10,000 variable features, while each
660 sample was treated as an individual batch. Cells were then integrated using n = 30 harmony-
661 corrected principal components, clustered at the resolution of 0.5 and then projected in 2D
662 space using uniform manifold approximation and projection (UMAP). Any clusters that
663 belonged to a non-myeloid lineage or had abnormally high levels of nuclear transcripts
664 (possibly damaged cells with intact nuclei) were discarded, leaving n=10,809 cells for
665 downstream analyses. Cluster marker genes and differentially expressed genes between
666 mouse groups were identified by the Wilcoxon rank-sum test implemented in the Seurat
667 package, and p-values were adjusted using the Benjamini-Hochberg procedure. Pathway
668 enrichment was performed using XGR[64]. Genes associated with oxidative phosphorylation
669 (OXPHOS) were obtained from the KEGG database and were converted to mouse symbols
670 using Ensembl genome database. OXPHOS scores were computed using the
671 "AddModuleScore" function in Seurat and normalized against a set of n=100 random control
672 genes.

673 The trajectory of osteoclast differentiation was recovered using information from RNA velocity.
674 In brief, genes with a minimum of 20 spliced and 20 unspliced transcripts were extracted from
675 the Cell Ranger alignment outputs and were analyzed in scVelo[22]. The splicing kinetics were
676 recovered using the dynamical model and n=500 top velocity genes. For consistency, we used
677 the same nearest-neighbor graph constructed from scRNA-seq data for all velocity analysis,
678 and inferred velocities were projected onto the scRNA-seq UMAP. The initial and terminal

bioRxiv preprint doi: https://doi.org/10.1101/2025.05.02.651799; this version posted August 2, 2025. The copyright holder for this preprint (which was not certified by peer review) is the author/funder. All rights reserved. No reuse allowed without permission.

679 clusters of the differentiation trajectory, together with a latent time for each cell, were inferred
680 using CellRank[23]. We used the default combination of a velocity kernel (80%, deterministic
681 mode) and a connectivity kernel (20%, computed based on the nearest-neighbor graph) to
682 compute the probabilities for cell-cell transitions. The cell-level transitional probabilities were
683 then aggregated at a cluster level and plotted as a fate map using directed PAGA[65].

684 For differential abundance test between BL/6^{C57}, and BL/6$^{C57\text{-}NZB}$ samples, batch-corrected
685 principal components were used to construct single-cell neighborhoods using MiloR[66], with
686 prop = 0.1, k=20 and d=30. In brief, cells from BL/6^{C57} or BL/6$^{C57\text{-}NZB}$ samples were counted
687 within each neighborhood, and the statistical significance of differential abundance was
688 evaluated using a generalized linear model with biological replicates included as covariates.
689 The test results were visualized on a UMAP using the "plotNhoodGraphDA" function.

690 Mitochondrial genotyping using single-cell RNA-seq data

691 Genetic variants in mitochondrial transcripts were recovered at single-cell level using the
692 mgatk pipeline[36]. In brief, sequencing reads were first aligned to a hard-masked mm10
693 reference genome using CellRanger (v7.1.0; 10x Genomics), followed by mgatk execution to
694 compute the per variant coverage across the mitochondrial genome. The per-cell
695 heteroplasmic ratio was calculated by dividing the summed allelic coverage of all variants
696 specific to NZB mitochondria (n=90, Supplementary Table 1) over the total sequencing
697 coverage at these locations. Only BL/6$^{C57\text{-}NZB}$ cells with more than 10 reads covering these
698 variants were retained (n=3,093) for downstream analyses.

699 Seahorse analyses

700 Metabolic assays were performed using a Seahorse XFe96 Analyzer with Seahorse XF Cell Mito
701 Stress Test Kit according to the manufacturer's instructions. Day 0, Day 1 and Day 3 pre-OCs
702 were seeded in a 96-well plate at the density of 25,000, 25,000and 15,000 cells per well. Cells
703 were treated with 10 ng/ml mouse M-CSF and 50 ng/ml mouse RANKL for indicated time prior
704 to the assay. A final concentration of 1 µM oligomycin, 2 µM FCCP and 1 µM Rotenone and
705 Antimycin A was used based on a pilot titration experiment. Cell density was quantified by
706 CyQuant staining post Seahorse for data normalization.

707 ATP Synthesis

708 ATP levels were quantified using the ATP Bioluminescence Assay Kit CLS II following the
709 manufacturer's protocol. Briefly, equal numbers of cells from each condition were pelleted,
710 boiled in Tris-EDTA buffer (pH 7.74) for 2 minutes, centrifuged, and the supernatant was
711 analyzed. Luminescence was measured in a CLARIOstar plate reader (BMG LABTECH).

712 Analysis of Complex I and Complex II Respiratory Activities

713 Enzymatic activities were measured spectrophotometrically using the Beer-Lambert law as
714 previously described[67]. Briefly, assays were conducted at 32°C with frozen-thawed
715 mitochondria in activity buffers. Complex I activity was initiated with 130 µM NADH and
716 monitored at 340 nm, subtracting rotenone-insensitive rates. NADH:O_2 and

bioRxiv preprint doi: https://doi.org/10.1101/2025.05.02.651799; this version posted August 2, 2025. The copyright holder for this preprint (which was not certified by peer review) is the author/funder. All rights reserved. No reuse allowed without permission.

717 NADH:decylubiquinone activities were assessed in sucrose buffer with specific inhibitors.
718 Complex II activity was measured at 600 nm after adding 10 mM succinate.

719 Western Blot Analyses

720 Autophagy flux during OC differentiation was assessed by incubating the cells in culture media
721 supplemented with 10 nM Bafilomycin A1 for 2 h, with DMSO served as the vehicle control.
722 Autophagic flux was calculated as the ratio of LC3-I to LC3-II.

723 Cell lysis was performed on ice using NP-40 lysis buffer containing proteinase inhibitors and
724 Phosphatase Inhibitor Cocktail 2. Afterward, the protein concentration was determined using
725 the Pierce™ BCA Protein Assay Kits. The lysate was then treated with Reducing Laemmli Sample
726 Buffer and 15–30 µg of proteins were loaded onto SDS-PAGE gels. For the separation of LC3-I
727 and LC3-II, a 15% Tris-HCl gel and SDS running buffer were employed, while NuPAGE Novex 4–
728 12% Bis-Tris gradient gels with NuPAGE™ MES SDS Running Buffer (1X) were used for other
729 proteins. Proteins were subsequently transferred to a PVDF membrane and blocked with 5%
730 skimmed milk-PBST. Primary antibodies were incubated overnight in 1% milk, followed by
731 secondary antibody incubation in 1% milk with 0.01% SDS for 1 hour. The following primary
732 antibodies were used: anti-LC3, anti-p62, anti-βActin and Total OXPHOS Rodent WB Antibody
733 Cocktail. Imaging was performed using the Odyssey CLx Imaging System, capturing the signals
734 from IRDye 800CW Donkey Anti-Rabbit IgG (H+L) (1:10,000 dilution) and IRDye 680RD Donkey
735 Anti-Mouse IgG (H+L) (1:10,000 dilution) simultaneously, with varying intensities based on
736 fluorescent exposure. See the Key resources table for a list of primary and secondary
737 antibodies. Data analysis was carried out using Image Studio Lite.

738 Confocal imaging

739 Bone marrow cells were seeded with 10 ng/ml mouse M-CSF and 50 ng/ml mouse RANKL and
740 differentiated for 1, 3, and 5 days in µ-Slide 18-well Ibidi chamber slides (81816, Ibidi GmbH).
741 Cells were fixed with 4% paraformaldehyde for 10 mins and permeabilized with 0.2% Triton X-
742 100 in PBS for another 10 minutes in room temperature. Cells were blocked with PBS
743 containing 2% BSA and 0.01% Tween20 for 1 h and incubated with the primary antibodies
744 overnight at 4 °C. The following antibodies were used to perform immunofluorescence staining
745 in murine and human cells: mouse anti-NDUFA9 (20C11B11B11), anti-NDUFB7 (Polyclonal),
746 anti-ATPβ (3D5), anti-TOMM20 (EPR15581-54). After washing with PBS for three times, cells
747 were incubated in 2% BSA-PBS for 1 hour with the following secondary antibodies: anti-mouse
748 IgG AF488, anti-mouse AF647, anti-mouse AF546, anti-rabbit AF488 and anti-rabbit AF568.
749 After washing with PBS and staining with 2 µg/ml DAPI for 10 minutes, coverslips were
750 mounted in SlowFade™ Diamond Antifade Mountant. Forty to eighty Z-stacks (0.13 µm) were
751 acquired using a Zeiss LSM 980 Airyscan2 confocal system and the ZenBlue software. Data were
752 analyzed using ImageJ/Fiji[68].

753 Genotyping and Heteroplasmy Analysis

754 Heteroplasmy levels were assessed as previously described[8]. Briefly, mice were genotyped at
755 postnatal day 21 using DNA extracted from ear notches with the REDExtract-N-Amp™ Tissue

bioRxiv preprint doi: https://doi.org/10.1101/2025.05.02.651799; this version posted August 2, 2025. The copyright holder for this preprint (which was not certified by peer review) is the author/funder. All rights reserved. No reuse allowed without permission.

756 PCR Kit. Additionally, DNA from cells undergoing OC differentiation (Day 0, Day 1, Day 3, and
757 Day 5) was isolated using 50 mM NaOH at 95°C, followed by neutralization with Tris-HCl (pH
758 7.5). The G4276A polymorphism, which introduces a BamHI restriction site in C57 mtDNA but
759 not in NZB mtDNA, was used for genotyping. DNA was PCR-amplified with REDExtract-N-Amp™
760 PCR ReadyMix using primers: Forward 5'-AAGCTATCGGGCCCATACCCCG-3' (3862-3884) and
761 Reverse 5'-GTTGAGTAGAGTGAGGGATGGG-3' (4503-4525), under the following conditions:
762 95°C (30s), 58°C (30s), 72°C (45s) for 30 cycles. The PCR product was digested with FastDigest
763 BamHI at 37°C for 20 minutes and analysed via agarose gel electrophoresis. DNA bands were
764 visualised using the Gel Doc XR+ System (Bio-Rad) and quantified with Quantity One Software.
765 The NZB mtDNA proportion was determined by the ratio of undigested 664-bp fragments to
766 the total of 664-bp (undigested) and 414/250-bp (digested) fragments, with heteroduplex
767 formation corrected using a standard curve from mixed C57 and NZB mtDNA samples.

768 Mitochondrial DNA copy number

769 Total DNA from cells undergoing osteoclast differentiation (Day 0, Day 1, Day 3, and Day 5) was
770 isolated using 50 mM NaOH at 95°C, followed by neutralization with Tris-HCl (pH 7.5). qRT-
771 PCR was performed on Applied Biosystems ®ViiA ™7 Real-Time PCR System using Power SYBR™
772 Green Master Mix in a 96-well plate to quantify mtDNA copy number relative to nDNA. The
773 primers used were mtCo2 (mtDNA): COII RTF (3'-CTACAAGACGCCACAT-5', 7037-7052) and COII
774 RTR (3'-GAGGGGGAGAGCAAT-5', 7253-7238), and SDH (nDNA): SDH RTF (3'-
775 TACTACAGCCCCAAGTCT-5', 1026-1043) and SDH RTR (3'-TGGACCCATCTTCTATGC-5', 1219-
776 1202). PCR conditions included an initial denaturation at 95°C for 2 min, followed by 40 cycles
777 of 95°C for 15 s and 60°C for 60 s, with a dissociation curve to confirm specificity. MtDNA copy
778 number was calculated as 2 × (2^ΔCt), with ΔCt = nCt - mtCt, which is inversely proportional to
779 mtDNA content[69].

780 Human osteoclast differentiation.

781 Human peripheral blood mononuclear cells (PBMCs) were isolated from EDTA-blood of healthy
782 donors and MELAS patients. The PBMCs were centrifuged and resuspended in 10% DMSO in
783 FBS and stored in -80° C. On the day of seeding (day -3), 2.5×10^5 cells/well of human PBMCs
784 were seeded in 96-well plates with 100 µL/well of Alpha-MEM culture media containing 100
785 ng/ml human M-CSF, 10% FBS, 1% pen/strep, and 1% L-glutamine. This setup was maintained
786 at 37°C in a 5.5% CO2 humidified incubator for 72 hours to facilitate the purification of
787 adherent cells through plastic adhesion. On day 0, the cells were induced to differentiate into
788 OCs in 100 µL/well of complete osteoclastogenic media (Alpha-MEM culture media with 10%
789 FBS, 1% pen/strep, and 1% L-glutamine) supplemented with 50 ng/ml human M-CSF and 100
790 ng/ml human RANKL, and spermidine at 10µM. Subsequently, the culture medium was
791 refreshed on day 2 and day 4. By day 6, mature OCs had formed and were fixed using 4% PFA
792 for TRAP analysis.

793

794

bioRxiv preprint doi: https://doi.org/10.1101/2025.05.02.651799; this version posted August 2, 2025. The copyright holder for this preprint (which was not certified by peer review) is the author/funder. All rights reserved. No reuse allowed without permission.

Statistical analysis

The mean ± standard error of the mean (SEM) was used to represent all data. When comparing two experimental groups, a two-tailed t-test was employed. For datasets that were normally distributed with equal variances, an unpaired two-tailed Student's t-test was utilized. In experiments that had ≥3 experimental groups, one-way analysis of variance (ANOVA) and multiple comparisons with Tukey's correction were employed. Paired or unpaired one-way ANOVA was utilized for multiple comparisons of normally distributed datasets with one variable. The p-value was applied to evaluate the statistical significance of the hypothesis being tested. GraphPad Prism (San Diego, CA, Version 9.5.1 (528)) was used for statistical analyses. Wilcoxon rank-sum tests were used in single-cell statistical testing in R (v4.2.2).

3D bone reconstruction

To reconstruct and visualize the bone, Algorithm 1 is used (Supplementary Table 1). First, the CT volumes are rotated and translated to a standard position and orientation. Next, binary volumes of the entire skeleton structure and the cortical bones are extracted from the input volumes through thresholding. Subsequently, the connected components in the binary volumes are counted. This step aids in removing the fibular bone and retaining the largest connected cortical bone, as facilitated by Algorithm 2. Thereafter, the largest cortical bone is dilated and then eroded to fill the hole inside the tibia using Algorithm 3. In the final step, the cortical bones with filled holes intersect with the tibial skeleton structure, excluding the fibula, to extract the 3D shape of the tibial bone in the region of interest.

In Algorithm 2, a binary volume V^i and the index k serve as inputs (Supplementary Table 2). The initial step involves identifying and counting the connected components using MATLAB's built-in function "bwconncomp()". In the subsequent step, the connected components within the binary volume are labeled and tallied using MATLAB's built-in functions "labelmatrix()" and "regionprops()". These connected components are then arranged in descending order using MATLAB's "sort()" function. The value of index k is assessed to determine whether it's positive or negative. If k is positive, the kth largest component is retained while others are discarded; if k is negative, the kth largest component is eliminated. The algorithm concludes by outputting the remaining components, V^o. As a result, this methodology is adept at removing the fibular bone and any extraneous fragments that lie outside the tibial bone.

Algorithm 3 takes a binary volume V^i and a series of iteration numbers for dilation or erosion $[t_1, t_2, \cdots t_k]$ as inputs (Supplementary Table 2). The structuring element is initialized using MATLAB's built-in function "strel()". Subsequently, for each iteration number designated for dilation or erosion, the iteration number t is examined. If t is positive, the copied binary volume V^o undergoes t dilation iterations, and if t is negative, V^o is eroded for t times. This algorithm is thus integrated into Algorithm 1 with the aim of filling holes inside the cortical bones and subsequently compressing the volume to adhere to the original bone size.

Quantification of OC from in vitro staining

bioRxiv preprint doi: https://doi.org/10.1101/2025.05.02.651799; this version posted August 2, 2025. The copyright holder for this preprint (which was not certified by peer review) is the author/funder. All rights reserved. No reuse allowed without permission.

To quantify the OC parameters from microscopic images, Algorithm 4 is employed to determine the area size and the ratio of the cell region. In Algorithm 4, each image is processed using its corresponding mask for the region of interest and specific thresholding values (Supplementary Table 2). The algorithm starts by normalizing the intensity of the input images. Subsequently, the red channel of the image is extracted through thresholding to identify and isolate the cell areas. The next step involves identifying and counting the connected components with MATLAB's built-in function “bwconncomp()”. Following that, the connected components within the binary image are labeled and enumerated using MATLAB's “labelmatrix()” and “regionprops()” functions. For each connected component, excluding the background region, the area size and its ratio in the entire region of interest are computed based on the areas of the red channels.

Acknowledgements

We acknowledge all Autophagy in the Immune System group members for their scientific discussions contributing to this manuscript and Prof. Jose Antonio Enríquez (Spanish National Center for Cardiovascular Research, CNIC, Madrid) who provided mouse models for our research and providing thoughtful feedback. We thank Dr. Hanlin Zhang from University of California, Berkeley for discussions and constructive comments. We thank Jianwei Cui from the University of Oxford who helped with experiments. We thank Patricia Cotta Moreira and Mino Medghalchi from the Kennedy Institute of Rheumatology animal facility, and the Barcelona Science Park (PCB) animal facility for their excellent care and assistance of animal well-being. We thank Thomas Conrad, Caroline Braeuning and Sarah Nathalie Vitcetz at the MDC Genomics Platform (BIH, Charité Campus Mitte, Berlin) for discussions about transcriptomic experiments and sequencing performed at their facility. Histology was performed in the Kennedy Institute of Rheumatology Histology Facility by Dr. Ida Parisi. We obtained confocal microscopy assistance from Christoffer Lagerholm, Senior Advanced Microscopy Manager at the Kennedy Institute of Rheumatology, and the Advanced Digital Microscopy (ADM) Core Facility at IRB Barcelona is greatly appreciated. We thank the NHS Highly Specialised Service for Rare Mitochondrial Disorders (Oxford University Hospitals, UK) for patient recruitment and for sharing clinical samples. We thank Dr. Elisabeth Greßler from Max-Delbrück-Center for Molecular Medicine for experimental assistance. Images were created using BioRender.com under the academic license granted to AKS.

This work was supported by: University of Oxford Medical and Life Sciences Translational Fund MC_PC_17174 and MC_PC_18059 from Wellcome ISSF fund to HL. China Scholarship Council fund (202006320024) to JJ. UMDF PF-23-0010 to RJ-M. Biotechnology and Biological Sciences Research Council (BBSRC, BB/X007049/1) to SM. Kennedy Trust Prize Studentship (AZT00050AZ04) to JZ. Chinese Academy of Medical Sciences (CAMS) Innovation Fund for Medical Sciences (CIFMS) 2018-I2M-2-002 to LL. Centre for OA Pathogenesis (Versus Arthritis 20205) to TLV. KTRR KENN202111 to AW. Oxford Hospitals charity and Lily Foundation “Treatments for Mitochondrial Disease – 2019/20” to JP. Salary support from the UK NHS

Specialist Commissioners who fund the “Rare Mitochondrial Disorders of Adults and Children” clinical Service to SDW. Novo Nordisk Foundation (NNF0064142) to COC. This work is funded by Diabetes UK (19/0005994 and 21/0006335), MRC (MR/T00200X/1) and Wellcome’s Institutional Strategic Support Fund awarded to University of Exeter; KAP and TH is funded by Wellcome Trust (219606/Z/19/Z); The work is supported by the National Institute for Health Research (NIHR) Exeter Biomedical Research Centre, Exeter, UK. European Molecular Biology Organization Postdoctoral Fellowship (EMBO) ALTF115-2019, “La Caixa” Foundation (ID 100010434, LCF/BQ/PI24/12040005), the Fundación Ramón Areces grant (Grant No. CIVP22A7576), and funding from MINECO through the Centers of Excellence Severo Ochoa Award and CERCA Programme of the Generalitat de Catalunya to AVL-V. Wellcome Trust Fund 220784/Z/20/Z to AKS.

Author contributions

AKS, A.V.L.-V. and H.L. conceptualized and designed the study.
A.V.L.-V., H.L., and J.J. performed and analyzed experiments, methodology, and investigation.
AKS, A.V.L.-V., H.L. and J.J. discussed analyses.
AKS and A.V.L.-V. supervised the project and interpreted the experimental data.
AKS, A.V.L.-V., H.L. and J.J. wrote the original draft.
AKS, A.V.L.-V., H.L., J.J. and TLV reviewed and edited the manuscript.
C.OC. planned experiments, analyzed data and edited the final manuscript.
K.G. performed mitochondrial DNA copy numbers, respiratory complexes activities and confocal imaging.
R.J-M. performed respiratory complexes analyses.
T.H. and K.A.P. investigated the association between m.3243A>G and bone parameters in individuals from the UK Biobank cohort.
J.Z. and TLV contributed to the 3D reconstructions of bone images and image analysis.
L.L. performed the isolation of donor PBMC samples, followed by OC differentiation, and autophagy flux assays.
S.W. and A.W. analyzed the bone stiffness parameters.
S.D.W. and J.P. provided samples and contributed to discussions on human and patient data.
All authors reviewed and approved the final manuscript.

Competing interests

The authors declare no competing interests.

References

1. Goto, Y., Nonaka, I. & Horai, S. A mutation in the tRNALeu(UUR) gene associated with the MELAS subgroup of mitochondrial encephalomyopathies. *Nature* **348**, 651–653 (1990).
2. Hirano, M. *et al.* MELAS: An original case and clinical criteria for diagnosis. *Neuromuscular Disorders* **2**, 125–135 (1992).

bioRxiv preprint doi: https://doi.org/10.1101/2025.05.02.651799; this version posted August 2, 2025. The copyright holder for this preprint (which was not certified by peer review) is the author/funder. All rights reserved. No reuse allowed without permission.

913 3. Gandhi, S. S., Muraresku, C., McCormick, E. M., Falk, M. J. & McCormack, S. E. Risk factors
914 for poor bone health in primary mitochondrial disease. *J of Inher Metab Disea* **40**, 673–
915 683 (2017).
916 4. Di Stadio, A. *et al.* Hearing impairment in MELAS: new prospective in clinical use of
917 microRNA, a systematic review. *Orphanet J Rare Dis* **13**, 35 (2018).
918 5. Handzel, O., Ungar, O. J., Lee, D. J. & Nadol, J. B. Temporal bone histopathology in MELAS
919 syndrome. *Laryngoscope Investig Oto* **5**, 152–156 (2020).
920 6. Fu, Y. *et al.* Engineering mtDNA deletions by reconstituting end joining in human
921 mitochondria. *Cell* S0092867425001941 (2025) doi:10.1016/j.cell.2025.02.009.
922 7. Latorre-Pellicer, A. *et al.* Mitochondrial and nuclear DNA matching shapes metabolism and
923 healthy ageing. *Nature* **535**, 561–565 (2016).
924 8. Lechuga-Vieco, A. V. *et al.* Cell identity and nucleo-mitochondrial genetic context modulate
925 OXPHOS performance and determine somatic heteroplasmy dynamics. *Sci. Adv.* **6**,
926 eaba5345 (2020).
927 9. Naue, J. *et al.* Evidence for frequent and tissue-specific sequence heteroplasmy in human
928 mitochondrial DNA. *Mitochondrion* **20**, 82–94 (2015).
929 10. Lechuga-Vieco, A. V. *et al.* Heteroplasmy of Wild-Type Mitochondrial DNA Variants in Mice
930 Causes Metabolic Heart Disease With Pulmonary Hypertension and Frailty. *Circulation* **145**,
931 1084–1101 (2022).
932 11. Sharpley, M. S. *et al.* Heteroplasmy of Mouse mtDNA Is Genetically Unstable and Results
933 in Altered Behavior and Cognition. *Cell* **151**, 333–343 (2012).
934 12. Ledesma-Colunga, M. G., Passin, V., Lademann, F., Hofbauer, L. C. & Rauner, M. Novel
935 Insights into Osteoclast Energy Metabolism. *Curr Osteoporos Rep* **21**, 660–669 (2023).

bioRxiv preprint doi: https://doi.org/10.1101/2025.05.02.651799; this version posted August 2, 2025. The copyright holder for this preprint (which was not certified by peer review) is the author/funder. All rights reserved. No reuse allowed without permission.

936 13. Lemma, S. *et al.* Energy metabolism in osteoclast formation and activity. *The International*
937 *Journal of Biochemistry & Cell Biology* **79**, 168–180 (2016).
938 14. Taubmann, J. *et al.* Metabolic reprogramming of osteoclasts represents a therapeutic
939 target during the treatment of osteoporosis. *Sci Rep* **10**, 21020 (2020).
940 15. Jiménez, J. A., Lawlor, E. R. & Lyssiotis, C. A. Amino acid metabolism in primary bone
941 sarcomas. *Front. Oncol.* **12**, 1001318 (2022).
942 16. Motyl, K. J., Guntur, A. R., Carvalho, A. L. & Rosen, C. J. Energy Metabolism of Bone. *Toxicol*
943 *Pathol* **45**, 887–893 (2017).
944 17. Zeng, R., Faccio, R. & Novack, D. V. Alternative NF-κB Regulates RANKL-Induced Osteoclast
945 Differentiation and Mitochondrial Biogenesis via Independent Mechanisms. *Journal of*
946 *Bone and Mineral Research* **30**, 2287–2299 (2015).
947 18. Harvey, J. N. & Barnett, D. Endocrine dysfunction in Kearns-Sayre syndrome. *Clinical*
948 *Endocrinology* **37**, 97–104 (1992).
949 19. Langdahl, J. H. *et al.* Mitochondrial Point Mutation m.3243A>G Associates With Lower
950 Bone Mineral Density, Thinner Cortices, and Reduced Bone Strength: A Case-Control Study.
951 *J Bone Miner Res* **32**, 2041–2048 (2017).
952 20. Leng, H. *et al.* Modulating glycosphingolipid metabolism and autophagy improves
953 outcomes in pre-clinical models of myeloma bone disease. *Nat Commun* **13**, 7868 (2022).
954 21. Latorre-Pellicer, A. *et al.* Regulation of Mother-to-Offspring Transmission of mtDNA
955 Heteroplasmy. *Cell Metab* **30**, 1120-1130.e5 (2019).
956 22. Bergen, V., Lange, M., Peidli, S., Wolf, F. A. & Theis, F. J. Generalizing RNA velocity to
957 transient cell states through dynamical modeling. *Nat Biotechnol* **38**, 1408–1414 (2020).
958 23. Lange, M. *et al.* CellRank for directed single-cell fate mapping. *Nat Methods* **19**, 159–170
959 (2022).

bioRxiv preprint doi: https://doi.org/10.1101/2025.05.02.651799; this version posted August 2, 2025. The copyright holder for this preprint (which was not certified by peer review) is the author/funder. All rights reserved. No reuse allowed without permission.

960 24. Ha, H. *et al.* Reactive oxygen species mediate RANK signaling in osteoclasts. *Experimental*
961 *Cell Research* **301**, 119–127 (2004).
962 25. Arnett, T. R. *et al.* Hypoxia is a major stimulator of osteoclast formation and bone
963 resorption. *Journal Cellular Physiology* **196**, 2–8 (2003).
964 26. Indo, Y. *et al.* Metabolic regulation of osteoclast differentiation and function. *J Bone Miner*
965 *Res* **28**, 2392–2399 (2013).
966 27. Zieliński, Ł. P., Smith, A. C., Smith, A. G. & Robinson, A. J. Metabolic flexibility of
967 mitochondrial respiratory chain disorders predicted by computer modelling.
968 *Mitochondrion* **31**, 45–55 (2016).
969 28. McKenzie, M., Lazarou, M., Thorburn, D. R. & Ryan, M. T. Analysis of mitochondrial subunit
970 assembly into respiratory chain complexes using Blue Native polyacrylamide gel
971 electrophoresis. *Analytical Biochemistry* **364**, 128–137 (2007).
972 29. Nolfi-Donegan, D., Braganza, A. & Shiva, S. Mitochondrial electron transport chain:
973 Oxidative phosphorylation, oxidant production, and methods of measurement. *Redox*
974 *Biology* **37**, 101674 (2020).
975 30. Wachter, C., Schatz, G. & Glick, B. S. Protein import into mitochondria: the requirement for
976 external ATP is precursor-specific whereas intramitochondrial ATP is universally needed for
977 translocation into the matrix. *Mol Biol Cell* **5**, 465–474 (1994).
978 31. Lazarou, M., McKenzie, M., Ohtake, A., Thorburn, D. R. & Ryan, M. T. Analysis of the
979 assembly profiles for mitochondrial- and nuclear-DNA-encoded subunits into complex I.
980 *Mol Cell Biol* **27**, 4228–4237 (2007).
981 32. Franco-Iborra, S. *et al.* Defective mitochondrial protein import contributes to complex I-
982 induced mitochondrial dysfunction and neurodegeneration in Parkinson's disease. *Cell*
983 *Death Dis* **9**, 1122 (2018).

bioRxiv preprint doi: https://doi.org/10.1101/2025.05.02.651799; this version posted August 2, 2025. The copyright holder for this preprint (which was not certified by peer review) is the author/funder. All rights reserved. No reuse allowed without permission.

984 33. Thomas, H. E. *et al.* Mitochondrial Complex I Activity Is Required for Maximal Autophagy.
985 *Cell Reports* **24**, 2404-2417.e8 (2018).
986 34. Kulawiak, B. *et al.* The mitochondrial protein import machinery has multiple connections
987 to the respiratory chain. *Biochimica et Biophysica Acta (BBA) - Bioenergetics* **1827**, 612–
988 626 (2013).
989 35. Park-Min, K.-H. Metabolic reprogramming in osteoclasts. *Semin Immunopathol* **41**, 565–
990 572 (2019).
991 36. Lareau, C. A. *et al.* Massively parallel single-cell mitochondrial DNA genotyping and
992 chromatin profiling. *Nat Biotechnol* **39**, 451–461 (2021).
993 37. Burgstaller, J. P. *et al.* MtDNA segregation in heteroplasmic tissues is common in vivo and
994 modulated by haplotype differences and developmental stage. *Cell Rep* **7**, 2031–2041
995 (2014).
996 38. Johnston, I. G. & Jones, N. S. Evolution of Cell-to-Cell Variability in Stochastic, Controlled,
997 Heteroplasmic mtDNA Populations. *Am J Hum Genet* **99**, 1150–1162 (2016).
998 39. Alsaleh, G. *et al.* Autophagy in T cells from aged donors is maintained by spermidine and
999 correlates with function and vaccine responses. *eLife* **9**, e57950 (2020).
1000 40. Puleston, D. J. *et al.* Autophagy is a critical regulator of memory CD8+ T cell formation. *eLife*
1001 **3**, e03706 (2014).
1002 41. Puleston, D. J. *et al.* Polyamines and eIF5A Hypusination Modulate Mitochondrial
1003 Respiration and Macrophage Activation. *Cell Metabolism* **30**, 352-363.e8 (2019).
1004 42. Al-Habsi, M. *et al.* Spermidine activates mitochondrial trifunctional protein and improves
1005 antitumor immunity in mice. *Science* **378**, eabj3510 (2022).
1006 43. Zhang, H. *et al.* Polyamines Control eIF5A Hypusination, TFEB Translation, and Autophagy
1007 to Reverse B Cell Senescence. *Molecular Cell* **76**, 110-125.e9 (2019).

bioRxiv preprint doi: https://doi.org/10.1101/2025.05.02.651799; this version posted August 2, 2025. The copyright holder for this preprint (which was not certified by peer review) is the author/funder. All rights reserved. No reuse allowed without permission.

1008 44. Chevalier, C. *et al.* Warmth Prevents Bone Loss Through the Gut Microbiota. *Cell*
1009 *Metabolism* **32**, 575-590.e7 (2020).
1010 45. Marques-Carvalho, A., Sardão, V. A., Kim, H.-N. & Almeida, M. ECSIT is essential for RANKL-
1011 induced stimulation of mitochondria in osteoclasts and a target for the anti-
1012 osteoclastogenic effects of estrogens. *Front. Endocrinol.* **14**, 1110369 (2023).
1013 46. Formosa, L. E., Dibley, M. G., Stroud, D. A. & Ryan, M. T. Building a complex complex:
1014 Assembly of mitochondrial respiratory chain complex I. *Semin Cell Dev Biol* **76**, 154–162
1015 (2018).
1016 47. Guerrero-Castillo, S. *et al.* The Assembly Pathway of Mitochondrial Respiratory Chain
1017 Complex I. *Cell Metab* **25**, 128–139 (2017).
1018 48. Hoefs, S. J. G. *et al.* Novel mutations in the NDUFS1 gene cause low residual activities in
1019 human complex I deficiencies. *Mol Genet Metab* **100**, 251–256 (2010).
1020 49. Jin, Z., Wei, W., Yang, M., Du, Y. & Wan, Y. Mitochondrial Complex I Activity Suppresses
1021 Inflammation and Enhances Bone Resorption by Shifting Macrophage-Osteoclast
1022 Polarization. *Cell Metabolism* **20**, 483–498 (2014).
1023 50. Spencer, J. A. *et al.* Direct measurement of local oxygen concentration in the bone marrow
1024 of live animals. *Nature* **508**, 269–273 (2014).
1025 51. Sun, C.-L., Van Gilst, M. & Crowder, C. M. Hypoxia-induced mitochondrial stress granules.
1026 *Cell Death Dis* **14**, 448 (2023).
1027 52. Krämer, L. *et al.* MitoStores: chaperone-controlled protein granules store mitochondrial
1028 precursors in the cytosol. *EMBO J* **42**, e112309 (2023).
1029 53. Buchan, J. R., Kolaitis, R.-M., Taylor, J. P. & Parker, R. Eukaryotic stress granules are cleared
1030 by autophagy and Cdc48/VCP function. *Cell* **153**, 1461–1474 (2013).

bioRxiv preprint doi: https://doi.org/10.1101/2025.05.02.651799; this version posted August 2, 2025. The copyright holder for this preprint (which was not certified by peer review) is the author/funder. All rights reserved. No reuse allowed without permission.

1031 54. Gwon, Y. *et al.* Ubiquitination of G3BP1 mediates stress granule disassembly in a context-
1032 specific manner. *Science* **372**, eabf6548 (2021).
1033 55. Hofer, S. J. *et al.* Spermidine is essential for fasting-mediated autophagy and longevity. *Nat*
1034 *Cell Biol* **26**, 1571–1584 (2024).
1035 56. Zhou, J. *et al.* Spermidine-mediated hypusination of translation factor EIF5A improves
1036 mitochondrial fatty acid oxidation and prevents non-alcoholic steatohepatitis progression.
1037 *Nat Commun* **13**, 5202 (2022).
1038 57. Messerer, J. *et al.* Spermidine supplementation influences mitochondrial number and
1039 morphology in the heart of aged mice. *J Anat* **242**, 91–101 (2023).
1040 58. Rossi, D., Kuroshu, R., Zanelli, C. F. & Valentini, S. R. eIF5A and EF -P: two unique translation
1041 factors are now traveling the same road. *WIREs RNA* **5**, 209–222 (2014).
1042 59. Dong, Y. *et al.* A clinical-stage Nrf2 activator suppresses osteoclast differentiation via the
1043 iron-ornithine axis. *Cell Metab* **36**, 1679-1695.e6 (2024).
1044 60. Kotrys, A. V. *et al.* Single-cell analysis reveals context-dependent, cell-level selection of
1045 mtDNA. *Nature* **629**, 458–466 (2024).
1046 61. Lake, N. J. *et al.* Quantifying constraint in the human mitochondrial genome. *Nature* **635**,
1047 390–397 (2024).
1048 62. Bakewell, S. J. *et al.* Platelet and osteoclast β_3 integrins are critical for bone metastasis.
1049 *Proc. Natl. Acad. Sci. U.S.A.* **100**, 14205–14210 (2003).
1050 63. Korsunsky, I. *et al.* Fast, sensitive and accurate integration of single-cell data with Harmony.
1051 *Nat Methods* **16**, 1289–1296 (2019).
1052 64. Fang, H., Knezevic, B., Burnham, K. L. & Knight, J. C. XGR software for enhanced
1053 interpretation of genomic summary data, illustrated by application to immunological traits.
1054 *Genome Med* **8**, 129 (2016).

bioRxiv preprint doi: https://doi.org/10.1101/2025.05.02.651799; this version posted August 2, 2025. The copyright holder for this preprint (which was not certified by peer review) is the author/funder. All rights reserved. No reuse allowed without permission.

1055 65. Wolf, F. A. *et al.* PAGA: graph abstraction reconciles clustering with trajectory inference
1056 through a topology preserving map of single cells. *Genome Biol* **20**, 59 (2019).
1057 66. Dann, E., Henderson, N. C., Teichmann, S. A., Morgan, M. D. & Marioni, J. C. Differential
1058 abundance testing on single-cell data using k-nearest neighbor graphs. *Nat Biotechnol* **40**,
1059 245–253 (2022).
1060 67. Curtabbi, A. *et al.* Regulation of respiratory complex I assembly by FMN cofactor targeting.
1061 *Redox Biology* **69**, 103001 (2024).
1062 68. Schindelin, J. *et al.* Fiji: an open-source platform for biological-image analysis. *Nat Methods*
1063 **9**, 676–682 (2012).
1064 69. Moreno-Loshuertos, R. *et al.* Differences in reactive oxygen species production explain the
1065 phenotypes associated with common mouse mitochondrial DNA variants. *Nat Genet* **38**,
1066 1261–1268 (2006).
1067

Figure Legends

Figure 1. Impaired OC differentiation in heteroplasmic cells, with maturation block emerging within the first three days

a Human PBMCs were seeded and differentiated into OCs using 50 ng/ml human M-CSF and 75 ng/ml human RANKL. Left: Representative images of TRAP staining from OC on day 9. Right: Quantification of the percentage of OC area relative to the total area. n=3 healthy donors (HD) and n=5 m.3243A>G patients; 3 technical replicates per condition. * $p < 0.05$, two-tailed unpaired t-test. Scale bar represents 100 µm.

b Bone marrow cells from 8-week-old mice BL/6^{C57}, BL/6^{NZB} and BL/6$^{C57\text{-}NZB}$ mice were differentiated into OCs using 10 ng/ml M-CSF and 50 ng/ml RANKL. OCs were identified by TRAP staining on day 5 (left), scale bar: 200 µm. The percentage of OC area relative to the total area was quantified (right). n= 20 mice per genotype (four independent experiments; each dot represents and individual animal). ****$p < 0.0001$ determined by one-way ANOVA test. Data are presented as mean ± SEM.

c UMAP visualization of 10,809 cells during OC differentiation, clustered by transcriptomic similarity and shown at day 0, day 1, and day 3 for different mtDNA groups (BL/6^{C57}, BL/6^{NZB}, and BL/6$^{C57\text{-}NZB}$).

d GO-BP pathway enrichment analysis for genes upregulated (red) or downregulated (blue) in BL/6$^{C57\text{-}NZB}$ OCs compared to BL/6^{C57} OCs.

Extended Data Figure 1. Single-cell transcriptomic profiling and trajectory analysis of OC formation

a Quantification of bone resorption marker CTX-1 levels in human serum samples from healthy donors (HD, n=10) and m.3243A>G patients (n=5). *$p < 0.05$, two-tailed unpaired t-test. Data are presented as mean values ± SEM.

b Schematic of experimental strategy for single-cell transcriptomics of murine OC formation. Bone marrow cells from BL/6^{C57} (n=3), BL/6^{NZB} (n=3), and BL/6$^{C57\text{-}NZB}$ (n=3) strains were isolated and cultured with M-CSF (50 ng/ml) for 2 days, followed by M-CSF (10 ng/ml) and RANKL (50 ng/ml) from day 0 to day 3. Single cell sequencing and analysis were then performed with day 0, day 1 and day 3 cells.

c Expression levels of OC marker genes (*Acp5* and *Ctsk*) from aggregated single cells at each time point, indicating successful *in vitro* osteoclastogenesis.

d Uniform manifold approximation and projection (UMAP) visualization of the expression levels of OCs marker genes (*Acp5*, *Mmp9, Ctsk, Dcstamp,* and *Ocstamp*) and negative regulators (*Irf8*, *Bcl6*, and *Mafb*). Color indicates log-normalized gene expression levels.

e UMAP visualization of single-cell transcriptomic profiles (n = 10,809 cells) during OC differentiation. Cells are clustered by transcriptomic similarity and shown at three time points: day 0, day 1 and day 3.

f UMAP projection of velocity-latent time estimated from the RNA splicing dynamics. Cells with a latent time of 0 or 1 represent the starting or terminating population inferred by RNA velocity, respectively.

g Fate map for OC differentiation using directed probabilistic approximate graph abstraction (PAGA). Each node represents one cluster, and arrows represent aggregated velocity flow concordant to the velocity-inferred trajectory. Dotted lines represent other velocity flow between each pair of clusters. Pie charts denote the relative abundance of $BL/6^{C57}$, $BL/6^{NZB}$ and $BL/6^{C57\text{-}NZB}$ cells, normalized by the total number of cells in each group. The relative abundance of $BL/6^{C57\text{-}NZB}$ cells for each cluster along the OC differentiation trajectory is labelled next to the pie chart.

h Differential abundance test representation. The relative enrichment of $BL/6^{C57\text{-}NZB}$ cells in early-stage pre-OCs (shown in red), as well as the relative depletion in mature OCs (shown in blue), indicates premature termination of osteoclastogenesis in heteroplasmic cells. Nodes represent neighborhoods of cells with similar transcriptomic profiles, colored by the relative abundance ($\log_2$FC) of $BL/6^{C57\text{-}NZB}$ cells compared to $BL/6^{C57}$. Node sizes correspond to the number of cells in a neighborhood. Non-significant neighborhoods ($p>0.05$) are colored in white and plotted in the background. The statistical significance of this observation was validated by differential abundance testing using MiloR.

Figure 2. OC profiling reveals metabolic and mitochondrial dysregulation during differentiation in heteroplasmic cells

a Heatmap showing gene expression changes in genes encoding subunits involved in ketogenesis, Krebs cycle, galactose metabolism, pentose phosphate, pyrimidine biosynthesis, adenosine biosynthesis and glycolysis in OCs derived from $BL/6^{C57\text{-}NZB}$ compared to $BL/6^{C57}$ mice at day 0, day 1, and day 3 (n=3 mice per genotype).

b Aggregated expression of OXPHOS genes (OXPHOS score) of *in vitro* OCs from different clusters (1-8) derived from $BL/6^{C57}$, $BL/6^{NZB}$, and $BL/^{6C57\text{-}NZB}$ mice (n=3 animals per genotype). Module expression scores were normalized by subtracting the aggregated expression levels of a randomly selected, expression matched control gene set.

c Oxygen consumption rate (OCR) profile of intact cells measured by Seahorse at days 0, 1, and 3 of OC differentiation (3-5 independent assays per biological replicate). Data are presented as mean values ± SEM.

d Heatmap showing gene expression changes for genes encoding respiratory Complex I in cells derived from BL/6$^{C57\text{-}NZB}$ compared to BL/6^{C57} mice at day 0, day 1, and day 3 of OC differentiation (n=3 mice per genotype).

e Total ATP levels measured by luminometry on days 1 and 3 of osteoclast differentiation in cells from BL/6^{C57}, BL/6^{NZB}, and BL/6$^{C57\text{-}NZB}$ mice. Each dot represents an individual mouse of the indicated genotypes. ** $p < 0.01$, determined using Tukey's multiple comparisons following two-way ANOVA.

f-g Confocal imaging of mitochondrial TOM20, Complex I subunit NDUFA9 and Complex V subunit ATPβ in pre-OCs on day 3 of differentiation derived from BL/6^{C57}, BL/6^{NZB}, and BL/6$^{C57\text{-}NZB}$ mice. **f**, Protein expression quantification ratio of NDUFA9 and ATPβ per mitochondrion (NDUFA9/TOM20; ATPβ/TOM20), based on marker signals (Integrated Density, IntDen) on day 3 (n=4 mice per genotype). **g**, Representative confocal images for the indicated markers. Scale bar: 5 µm, n = 4 mice per genotype. * $p <0.05$, two-tailed Dunnett's test following one-way ANOVA. Data are presented as mean values ± SEM.

Extended Data Figure 2. Analysis of mtDNA-encoded genes, respiratory complexes, and bioenergetic parameters during OC differentiation

a Violin plots displaying the average expression levels of mitochondrial DNA-encoded genes in BL/6^{C57} cells at day 0 (n = 1,550), day 1 (n = 1,148), and day 3 (n = 1,292) during OC differentiation. Complex I: mt-Nd1, mt-Nd2, mt-Nd3, mt-Nd4, mt-Nd4L, mt-Nd5 and mt-Nd6. Complex III: mt-Cytb. Complex IV: mt-Co1, mt-Co2 and mt-Co3. Complex V (ATPase): mt-Atp6 and mt-Atp8. The y-axis represents the depth-normalized gene expression level in log scale (log count per 10,000 sequencing reads). **** $p < 0.0001$, Wilcoxon test, with day 0 and day 1 cells as the reference groups.

b Spare respiratory capacity (SRC) calculated by subtracting basal respiration from maximal respiration during *in vitro* OC differentiation (day 0 to day 3) for the indicated genotypes (n=5, two independent experiments). *$p < 0.05$, two-tailed Dunnett's test following one-way ANOVA. Data are presented as mean ± SEM.

c Mitochondrial content was assessed using N-acridine orange (NAO) staining. Live cells were analyzed by FACS during OC differentiation from day 0 to day 3. n= 3 BL/6^{C57} n=3 BL/6^{NZB} and n=5 BL/6$^{C57\text{-}NZB}$. * $p<0.05$, determined using Tukey's multiple comparisons following two-way ANOVA. Data are normalized to wild-type BL/6^{C57} and presented as mean ± SEM.

d ROS quantification on day 0, day 1 and day 3 during OC differentiation. Left: Quantification of CellROX Deep Red MFI measurements. Right: FACS histogram plot are representative measurements on day 1 from cells derived from BL/6^{C57} (blue), BL/6^{NZB} (red) BL/6$^{C57\text{-}NZB}$ (green) mice, where the grey line shows background MFI (unstained). n= 3 BL/6^{C57} n=3 BL/6^{NZB} and n=5 BL/6$^{C57\text{-}NZB}$. * $p<0.05$, ** $p<0.01$ determined using Tukey's multiple comparisons following two-way ANOVA. Data are normalized to wild-type BL/6^{C57} and presented as mean ± SEM.

e Western blot analysis for OXPHOS complexes protein expression in day 0, day 1 and day 3 of *in vitro* OC differentiation. CI-NDUFB8, CII-SDHB, CIII-UQCRC2, CIV-MTCO1 and CV-ATP5A levels are shown. TOM20 expression was used as mitochondrial protein loading control. Representative image from four independent experiments, n=4 mice per genotype.

f Ratio of Complex I to Complex II activities. Respiratory complexes activities were measured spectrophotometrically using 5 µg of total mitochondrial protein per assay. Measurements were performed in four replicates using pre-OCs on days 0 and 3 of differentiation. n= 4 mice per genotype. ** $p<0.01$, Dunnett's test following one-way ANOVA. Data are presented as mean ± SEM.

g Confocal imaging of mitochondrial TOM20 (red), Complex I subunit NDUFA9 (cyan) and DAPI (grey) in pre-OCs on day 1 of differentiation derived from BL/6^{C57}, BL/6^{NZB}, and BL/6$^{C57\text{-}NZB}$ mice. Representative confocal images for the indicated markers. Scale bar: 5 µm, n = 4 mice per genotype.

Figure 3. Impaired import of nuclear-encoded complex I subunits disrupts complex assembly and function in heteroplasmic cells

a-b: Confocal imaging of mitochondrial TOM20, Complex I subunit NDUFA9 and DAPI in pre-OCs on day 3 of differentiation (**a**) and mature OCs on day 5 of differentiation (**b**) derived from BL/6^{C57}, BL/6^{NZB}, and BL/6$^{C57\text{-}NZB}$ mice. Left: Representative confocal images for the indicated markers. Right: Quantification of colocalization of Complex I in the mitochondria (TOM20/NDUFA9) using as a control colocalization between mitochondria and the nucleus (TOM20/DAPI), shown by Pearson's coefficient. Scale bar: 5 µm, n = 4 mice per genotype. * $p<0.05$, *** $p < 0.001$, **** $p < 0.00001$, two-tailed Dunnett's test following one-way ANOVA. In **a-b**, data are presented as mean values ± SEM.

c-e Heatmap showing gene expression changes for genes involved in the mitochondrial protein import machinery (**c**), mitochondrial degradome (**d**) and mitochondrial assembly factors (**e**) in OCs cultures derived from BL/6$^{C57\text{-}NZB}$ and BL/6^{C57} mice at day 0, day 1, and day 3 (n=3 mice per genotype).

Figure 4. OC differentiation relies on sustained autophagy during early stages, with mtDNA selection required in heteroplasmic cells

a NZB mtDNA levels (estimated as a percentage of total mtDNA) from BL/6$^{C57\text{-}NZB}$ mice, showing a shift toward the NZB haplotype in day 3 cells compared to day 1. Each dot represents one cell and is colored by the percentile-normalized sequencing coverage of NZB mtDNA variants. The color scale represents sequencing depth. Day 1: n = 1,249 cells. Day 3: n = 884 cells. Median values are marked by black lines. **** $p < 0.0001$, Wilcoxon test.

b Assessment of the heteroplasmy shift toward NZB mtDNA at day 3 compared to day 1 in pre-OCs derived from BL/6$^{C57\text{-}NZB}$ young mice (n=9; each dot represents an individual mouse). The transformed heteroplasmy shift was evaluated using day 0 as the reference for each heteroplasmic mouse. NZB mtDNA levels were obtained by PCR, followed by RFLP (Restriction Fragments Length Polymorphism) to distinguish between C57 and NZB mtDNA variants. * $p < 0.05$, unpaired t test. Data are presented as mean values ± SEM.

c NZB mtDNA levels in BL/6$^{C57\text{-}NZB}$ cells across different clusters indicating increased NZB mtDNA selection in OCs compared to monocytic precursors. Median values are marked by grey lines. **** $p < 0.0001$, Wilcoxon test, with monocytic precursors as the reference group.

d-e Western Blot analysis of autophagy in primary murine BM cells treated with M-CSF and RANKL for 1 or 3 days. **d,** Representative images of membranes showing p62 and LC-3 expression. **e,** autophagy flux quantification of the LC-3 bands (LC3-I/LC3-II) at day 1 and 3 of OC differentiation. 10 nM BafA1 was added 2 hours before protein harvest, with actin used as a protein loading control. n = 8 independent biological samples for DMSO control and BafA. **$p < 0.01$, ****$p < 0.0001$, two-way ANOVA with Sidak's multiple comparisons test. Data are presented as mean values ± SEM.

Extended Data Figure 3. Analysis of mitochondrial selection and the role of autophagy during OC maturation

a Average sequencing depth (bars) and the average heteroplasmic percentage (dots) for selected NZB mtDNA variants in heteroplasmic cells. Colors represent the number of cells with at least 10x coverage for a given variant.

b NZB mtDNA levels (%NZB mtDNA, y axis) plotted against the velocity latent time (x axis, same latent time as shown in **Extended Data Fig.1f**), demonstrating a slight shift towards NZB mtDNA during OC differentiation. *** $p < 0.001$, Spearman's rank correlation test.

c Assessment of the percentage of NZB mtDNA (% NZB mtDNA) during *in vitro* OC differentiation of heteroplasmic cells (0, 48, and 192 hours after the addition of 10 ng/ml M-CSF and 50 ng/ml RANKL). NZB mtDNA levels were quantified by PCR, followed by RFLP (Restriction Fragment Length Polymorphism) to distinguish between C57 and NZB mtDNA variants. Samples were derived from n = 4 BL/6$^{C57\text{-}NZB}$ mice.

d NZB mtDNA levels (%NZB mtDNA, y axis) in the OC cluster (cluster 2) at day 0, day 1 and day 3 of differentiation. * $p < 0.05$, Wilcoxon Rank Sum test.

e Quantification of p62 expression from Western blot analyses shown in **Fig.4d**. Actin was used as a protein loading control. n = 6 independent biological samples for DMSO control and BafA1; each dot represents an individual mouse. **$p < 0.01$, determined using Tukey's multiple comparisons following two-way ANOVA. Data are presented as mean values ± SEM.

Figure 5. Spermidine enhances cellular ATP levels and restores osteoclast differentiation in murine and human heteroplasmic cells

a-b Bone marrow cells from 8-week-old BL/6^{C57}, BL/6^{NZB} and BL/6$^{C57\text{-}NZB}$ mice were differentiated into OCs using 10 ng/ml M-CSF and 50 ng/ml RANKL with or without 10 uM spermidine (spd) treatment. **a,** OCs were identified by TRAP staining on day 5. Scale bar: 50 µm. **b,** percentage of OC area relative to the total area was quantified. Data are representative of two independent experiments. * $p < 0.05$, **** $p < 0.0001$, nonparametric Kruskal-Wallis test. Data are presented as mean values ± SEM.

c Assessment of the heteroplasmy shift toward NZB mtDNA at day 5 in OCs derived from BL/6$^{C57\text{-}NZB}$ young mice (n=10 for untreated and n=8 for cultures treated with 10 µM spermidine; each dot represents an individual mouse). The transformed heteroplasmy shift was evaluated using day 1 as the reference for each heteroplasmic mouse. NZB mtDNA levels were quantified by PCR, followed by RFLP (Restriction Fragments Length Polymorphism) to distinguish between C57 and NZB mtDNA variants. ** $p < 0.01$, nonparametric Mann-Whitney test. Data are presented as mean values ± SEM.

d Total ATP levels were measured by luminescence on day 3 of OC differentiation in cells from BL/6^{C57}, BL/6^{NZB}, and BL/6$^{C57\text{-}NZB}$ mice, with and without 10 µM spermidine treatment. Data are normalized to untreated cells and each dot represents a sample from an individual mouse of the indicated genotype. **** $p < 0.0001$, one-way ANOVA and Sidak's multiple comparison test. Data are presented as mean values ± SEM.

e Confocal imaging of mitochondrial TOM20, Complex I subunit NDUFA9, and ATPase subunit ATPβ in OCs derived from BL/6^{C57}and BL/6^{NZB}, and BL/6$^{C57\text{-}NZB}$ mice with and without spermidine treatment on day 5 of *in vitro* OC differentiation. Left: Protein

quantification ratio of NDUFA9 per mitochondrion (NDUFA9/TOM20), based on marker signals (Integrated Density, IntDen) (n=3 mice per genotype). ** p <0.01, *** p <0.001, two-tailed Dunnett's test following one-way ANOVA. Data are presented as mean values ± SEM. Right: Representative confocal images for the indicated markers in pre-OCs derived from BL/6$^{C57\text{-}NZB}$ mice with and without spermidine treatment on day 5 of *in vitro* OC differentiation. Scale bar: 5 µm.

f Human PBMCs were seeded and differentiated into OCs in the presence of 50 ng/ml human M-CSF and 75 ng/ml human RANKL, with or without 10 µM spermidine treatment. Left: Representative images of TRAP staining from OC on day 6. Scale bar: 50 µm. Right: Quantification of the percentage of OC area relative to the total area. n=4 healthy donors (HD) and n=4 m.3243A>G patients; 6 technical replicates per condition. ** p < 0.01, determined using Tukey's multiple comparisons following one-way ANOVA. Data are presented as mean values ± SEM.

g Total ATP levels assessed by luminescence on day 5 of OC differentiation in cells derived from human PBMCs in the presence of 50 ng/ml human M-CSF and 75 ng/ml human RANKL, with or without 10 µM spermidine treatment. Each dot represents *in vitro* OC differentiation from a donor. n=5 healthy donors (HD) and n=5 m.3243A>G patients. * p < 0.05, determined using Tukey's multiple comparisons following one-way ANOVA. Data are presented as mean values ± SEM.

Extended Data Figure 4. Spermidine enhances mtDNA selection and complex I expression in heteroplasmic cells

a Mitochondrial DNA copy numbers in BL/6$^{C57\text{-}NZB}$ cell cultures without (Control) or with 5 µM spermidine treatment (+Spd) on day 1 and day 3 during OC differentiation (n=4-5 mice). MtDNA copy numbers were normalized to genomic DNA copy numbers, as determined by qPCR (2−ΔCT). Data are presented as mean values ± SEM.

b Total ATP levels were measured by luminometry on day 1 of OC differentiation in cells derived from BL/6^{C57}, BL/6^{NZB}, and BL/6$^{C57\text{-}NZB}$ mice, with and without 10 µM spermidine treatment. Data are normalized to untreated cells and each dot represents a sample from an individual mouse of the indicated genotype. Data are presented as mean values ± SEM.

c-d Confocal imaging of mitochondrial TOM20, Complex I subunit NDUFA9, and ATPase subunit ATPβ in OCs derived from BL/6^{C57}and BL/6^{NZB}, and BL/6$^{C57\text{-}NZB}$ mice with and without spermidine treatment on day 5 of *in vitro* OC differentiation. **c,** Protein quantification ratio of ATPβ per mitochondrion (ATPβ/TOM20), based on marker signals (Integrated Density, IntDen) (n=3 mice per genotype). **** p <0.0001, *** p <0.001, ** p

<0.01, two-tailed Dunnett's test following one-way ANOVA. Data are presented as mean values ± SEM.**d,** Representative confocal images for the indicated markers in OCs derived from BL/6^{C57}and BL/6^{NZB} mice with and without spermidine treatment on day 5 of *in vitro* OC differentiation. Scale bar: 5 µm.

Figure 6. OC dysfunction drives increased bone density in heteroplasmic mice, reversed by spermidine treatment

a Representative TRAP/0.2% methyl green-stained tibial sections showing OCs (red/purple, black arrowheads) on the endocortical bone surface in BL/6^{C57}, BL/6^{NZB} and BL/6$^{C57\text{-}NZB}$ mice (n=5, two independent experiments). Scale bar: 200 µm.

b Bone histomorphometric quantification of OCs: percentage of OC surface relative to the total bone surface (Oc.S/BS) (BL/6^{C57}, $n = 10$; BL/6^{NZB}, $n = 9$; and BL/6$^{C57\text{-}NZB}$, $n = 10$ mice, each dot represents an individual animal). * $p < 0.05$, one-way ANOVA followed by Tukey's multiple comparisons test.Data are presented as mean ± SEM.

c-d ELISA analysis of serum levels of CTX-1 (**c**) (BL/6^{C57}, $n = 16$; BL/6^{NZB}, $n = 16$; and BL/6$^{C57\text{-}NZB}$, $n = 16$ mice) and PINP (**d**) (BL/6^{C57}, $n = 10$; BL/6^{NZB}, $n = 8$; and BL/6$^{C57\text{-}NZB}$, $n = 10$ mice), each dot represents an individual animal. * $p < 0.05$, one-way ANOVA followed by Tukey's multiple comparisons test.Data are presented as mean ± SEM.

e Representative micro-CT reconstructed images of tibiae from 12-week-old male BL/6^{C57}, BL/6^{NZB} and BL/6$^{C57\text{-}NZB}$ mice.

f–**g** Micro-CT analysis of trabecular and cortical bone morphology parameters: (**f**) BV/TV (bone volume fraction), Tb.Th (trabecular thickness), BS/BV (bone surface density), Tb.Sp (trabecular separation); (**g**) Ct.Th (cortical thickness) and Ct.Ar (cortical area) (BL/6^{C57}, $n = 9$; BL/6^{NZB}, $n = 12$; and BL/6$^{C57\text{-}NZB}$, $n = 10$; each dot represents tibial measurements from an individual animal). * $p < 0.05$, ** $p < 0.01$, *** $p < 0.001$, **** $p < 0.0001$, one-way ANOVA followed by Tukey's multiple comparisons test. Data are presented as mean ± SEM.

h-i Schematic overview illustrating the positioning of femur for compression testing between the load area and the platform load frame (**h, left**). Representative load displacement curve of femur from the BL/6^{C57} control group (**h, right**). Dot plot showing the maximum load values for the femur in 12- to 14-week-old males of the indicated genotypes (**i**). BL/6^{C57}, $n = 8$; BL/6^{NZB}, $n = 8$; and BL/6$^{C57\text{-}NZB}$, $n = 7$. Each dot represents femoral measurements from an individual animal. ** $p < 0.01$, *** $p < 0.001$, one-way ANOVA followed by Tukey's multiple comparisons test. Data are presented as mean ± SEM.

j-k Lethally irradiated 8-week-old CD45.1+ B6.SJL and BL/6$^{C57\text{-}NZB}$ CD45.1+ mice were reconstituted with BM cells from BL/6^{C57} CD45.2+ or BL/6$^{C57\text{-}NZB}$ CD45.2+ mice. After 9 weeks, micro-CT analysis was performed on tibiae. **j,** Representative micro-CT reconstructed images. **k,** BV/TV quantification (BL/6^{C57} to CD45.1+ B6.SJL, n = 10; BL/6$^{C57\text{-}NZB}$ to CD45.1^{+} B6.SJL, n = 12; BL/6^{C57} to BL/6$^{C57\text{-}NZB}$, n = 10; BL/6$^{C57\text{-}NZB}$ to BL/6$^{C57\text{-}NZB}$, n = 8; each dot represents an individual animal). *$p < 0.05$, two-way ANOVA. Data are presented as mean values ± SEM.

l-m Lethally irradiated young BL/6$^{C57\text{-}NZB}$ mice were reconstituted with bone marrow from BL/6^{C57} or BL/6$^{C57\text{-}NZB}$ mice and treated with 5 mM spermidine in drinking water for 8 weeks. **l,** Representative micro-CT reconstructed images of tibiae from the bone marrow reconstituted mice. **m,** BV/TV of tibiae quantification by micro-CT (n = 8 BL/6^{C57}; n = 6 BL/6$^{C57\text{-}NZB}$ and n = 7 BL/6$^{C57\text{-}NZB}$ + Spd; each dot represents an individual animal). The experiment is representative of two independent experiments. ** $p < 0.01$, one-way ANOVA followed by Tukey's multiple comparisons test. Data are presented as mean ± SEM.

n Bending test analysis in bone marrow transplanted mice treated with 5 mM spermidine. Dot plots of maximum femur load from bone marrow-transplanted mice, assessed using the bending test (n = 5 mice per BM cell genotype; each dot represents an independent animal). *$p < 0.05$, **$p < 0.01$, one-way ANOVA followed by Tukey's multiple comparisons test. Data are presented as mean ± SEM.

Extended Data Figure 5. OC progenitor gating, chimera reconstitution, and bone analysis

a Flow cytometry gating strategy of the OC progenitors (CD11b- B220- CD3- CD115+) in BM cells (left) and percentage of OC progenitors (right) from BL/6^{C57} mice (n=10), BL/6^{NZB} mice (n=8) and BL/6$^{C57\text{-}NZB}$ (n=9) mice. Data are presented as mean ± SEM.

b Assessment of reconstitution efficacy in chimeric mice by evaluating the BM CD45.2+ population. Each dot represents an individual animal. Filled dots: donor cells; Empty dots: endogenous cells.

c Representative flow cytometry plots showing the gating strategy and distribution of CD45.1+/CD45.2+ BM cells from the specified groups.

d Morphological bone parameters in tibiae measured by micro-CT. Tb.Th, BS/BV, Tb.Sp, Ct.Th and Ct.Ar (BL/6^{C57} to CD45.1+ B6.SJL group (n=10); BL/6$^{C57\text{-}NZB}$ to CD45.1^{+} B6.SJL group (n=12); BL/6^{C57} to BL/6$^{C57\text{-}NZB}$ group (n=10); BL/6$^{C57\text{-}NZB}$ to BL/6$^{C57\text{-}NZB}$ group (n=8). Each dot represents and individual animal. *$p < 0.05$, **$p < 0.01$; ***$p < 0.001$, determined by two-way ANOVA test. Data are presented as mean ± SEM.

e Lethally irradiated young BL/6$^{C57\text{-}NZB}$ mice were reconstituted with bone marrow from BL/6^{C57} or BL/6$^{C57\text{-}NZB}$ mice and treated with 5 mM spermidine in drinking water for 8 weeks. Tb.Th, BS/BV Tb.Sp, Ct.Th and Ct.Ar of tibiae quantification by micro-CT (n = 8 BL/6^{C57}; n = 6 BL/6$^{C57\text{-}NZB}$ and n = 7 BL/6$^{C57\text{-}NZB}$ + Spd; each dot represents an individual animal). The experiment is representative of two independent experiments. *$p < 0.05$, **$p < 0.01$, ***$p < 0.001$, ****$p < 0.0001$, one-way ANOVA followed by Tukey's multiple comparisons test.

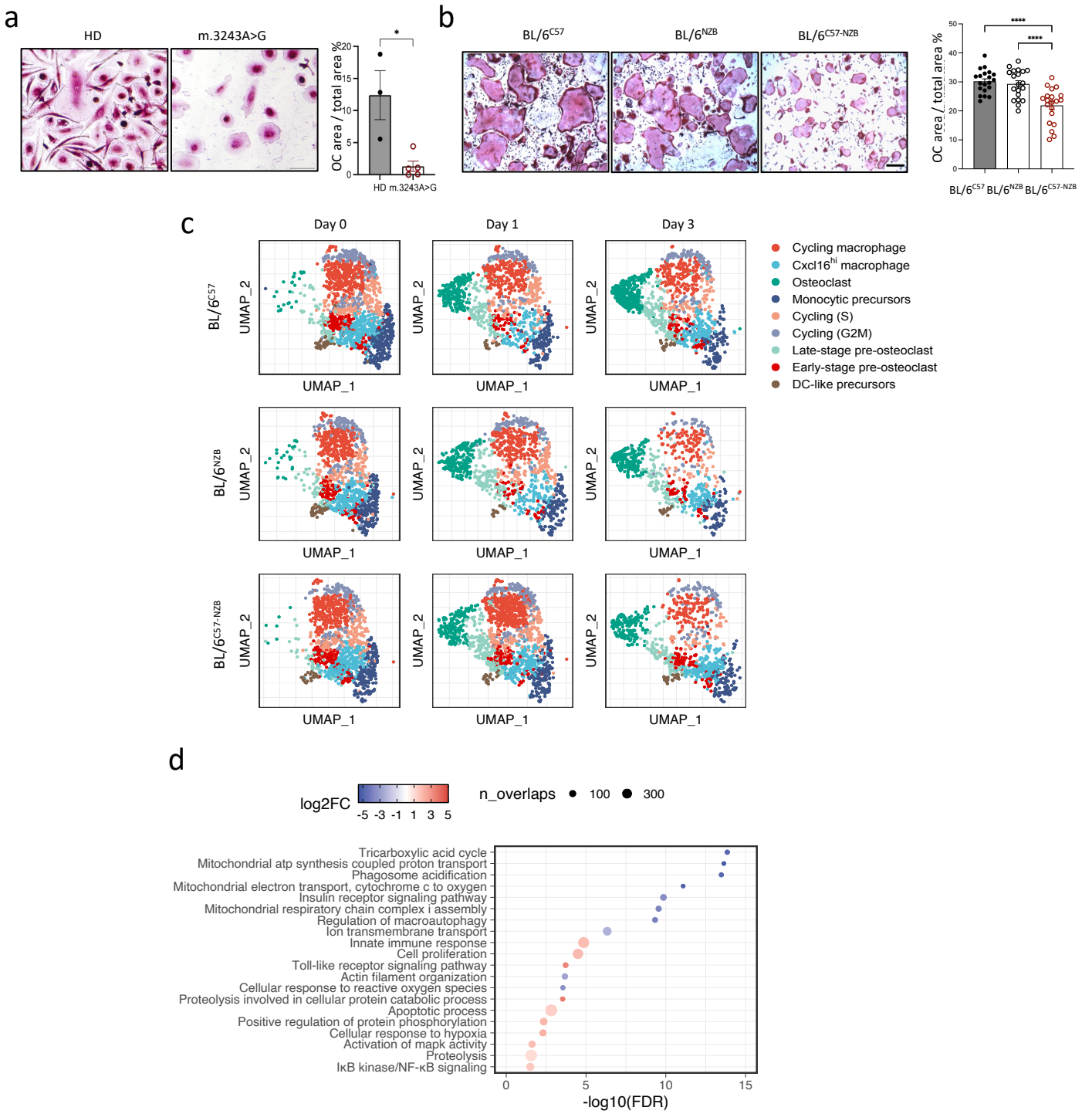
a
HD
m.3243A>G
OC area / total area %
HD m.3243A>G
b
BL/6C57
BL/6NZB
BL/6C57-NZB
OC area / total area %
c
Day 0
Day 1
Day 3
BL/6C57
BL/6NZB
BL/6C57-NZB
UMAP_1
UMAP_2
Cycling macrophage
Cxcl16hi macrophage
Osteoclast
Monocytic precursors
Cycling (S)
Cycling (G2M)
Late-stage pre-osteoclast
Early-stage pre-osteoclast
DC-like precursors
d
log2FC
n_overlaps
Tricarboxylic acid cycle
Mitochondrial atp synthesis coupled proton transport
Phagosome acidification
Mitochondrial electron transport, cytochrome c to oxygen
Insulin receptor signaling pathway
Mitochondrial respiratory chain complex i assembly
Regulation of macroautophagy
Ion transmembrane transport
Innate immune response
Cell proliferation
Toll-like receptor signaling pathway
Actin filament organization
Cellular response to reactive oxygen species
Proteolysis involved in cellular protein catabolic process
Apoptotic process
Positive regulation of protein phosphorylation
Cellular response to hypoxia
Activation of mapk activity
Proteolysis
IκB kinase/NF-κB signaling
-log10(FDR)

Figure 1

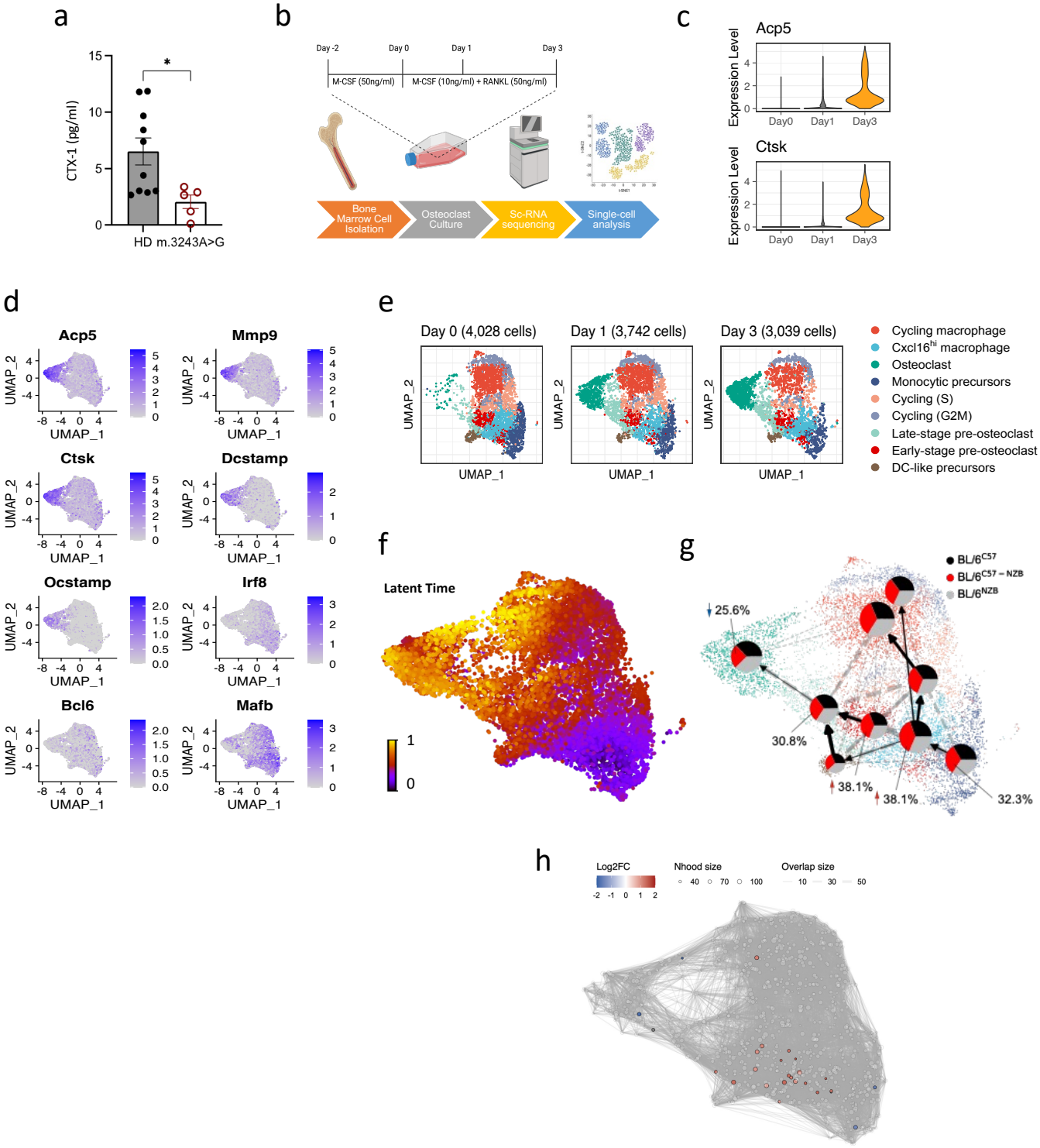

Extended Data Fig. 1

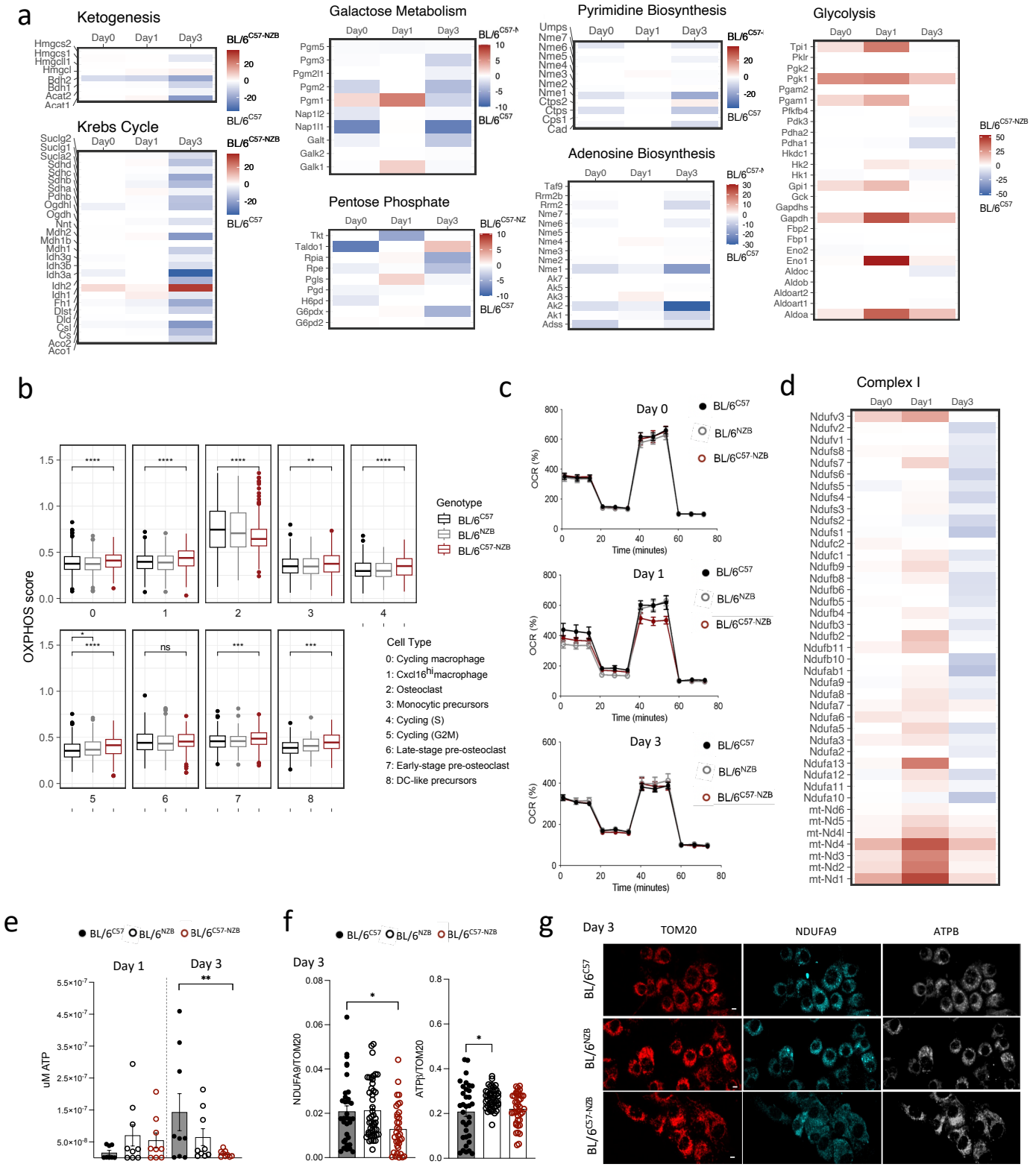
a
Ketogenesis
Krebs Cycle
Galactose Metabolism
Pentose Phosphate
Pyrimidine Biosynthesis
Adenosine Biosynthesis
Glycolysis
Day0
Day1
Day3
BL/6C57-NZB
BL/6C57
b
OXPHOS score
Genotype
BL/6C57
BL/6NZB
BL/6C57-NZB
Cell Type
0: Cycling macrophage
1: Cxcl16hi macrophage
2: Osteoclast
3: Monocytic precursors
4: Cycling (S)
5: Cycling (G2M)
6: Late-stage pre-osteoclast
7: Early-stage pre-osteoclast
8: DC-like precursors
c
Day 0
Day 1
Day 3
OCR (%)
Time (minutes)
d
Complex I
e
Day 1
Day 3
uM ATP
f
Day 3
NDUFA9/TOM20
ATPβ/TOM20
g
Day 3
TOM20
NDUFA9
ATPB

Figure 2

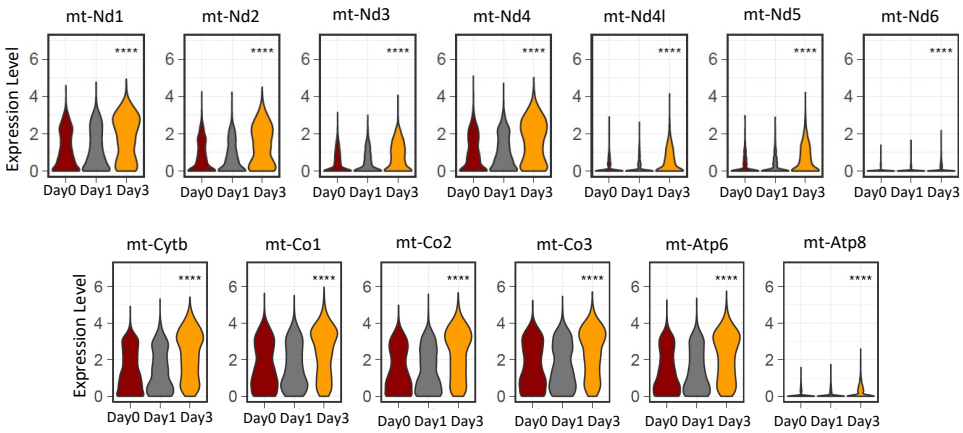

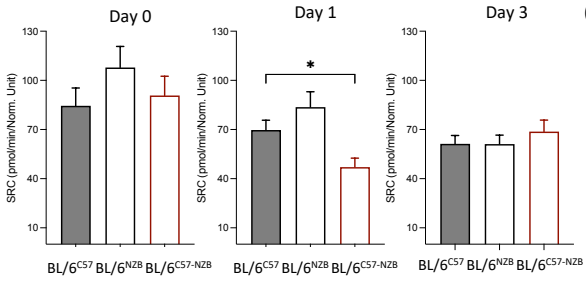

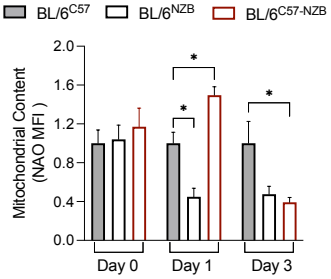

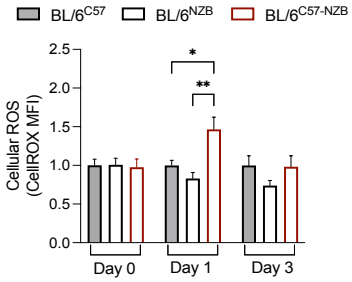

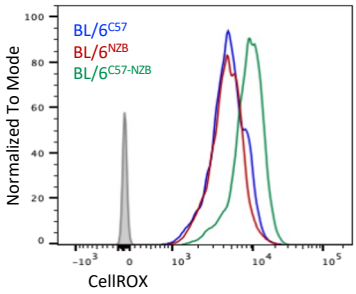

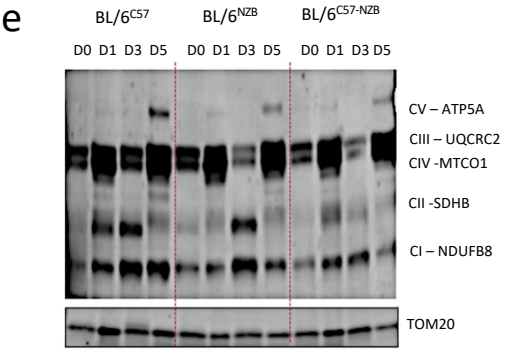

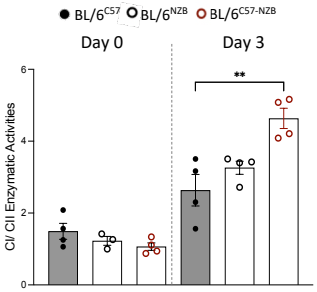

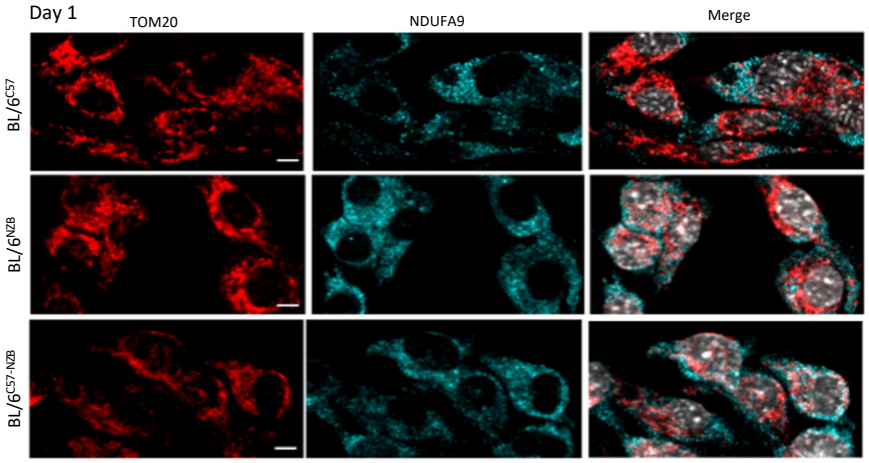

Extended Data Fig. 2

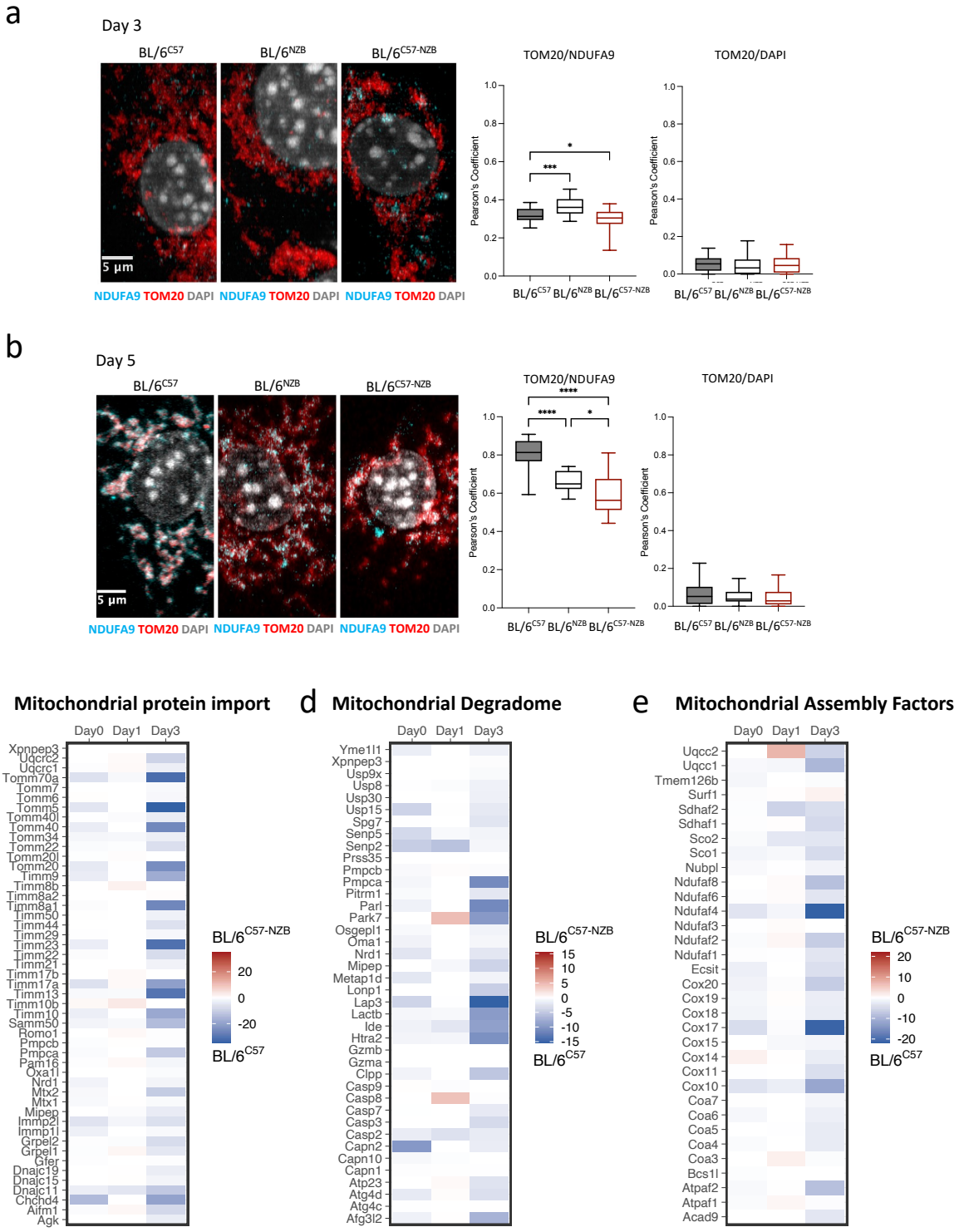
a
Day 3
BL/6C57
BL/6NZB
BL/6C57-NZB
5 µm
NDUFA9 TOM20 DAPI NDUFA9 TOM20 DAPI NDUFA9 TOM20 DAPI
TOM20/NDUFA9
TOM20/DAPI
Pearson's Coefficient
BL/6C57 BL/6NZB BL/6C57-NZB
b
Day 5
c Mitochondrial protein import
d Mitochondrial Degradome
e Mitochondrial Assembly Factors
Day0 Day1 Day3
BL/6C57-NZB
BL/6C57

Figure 3

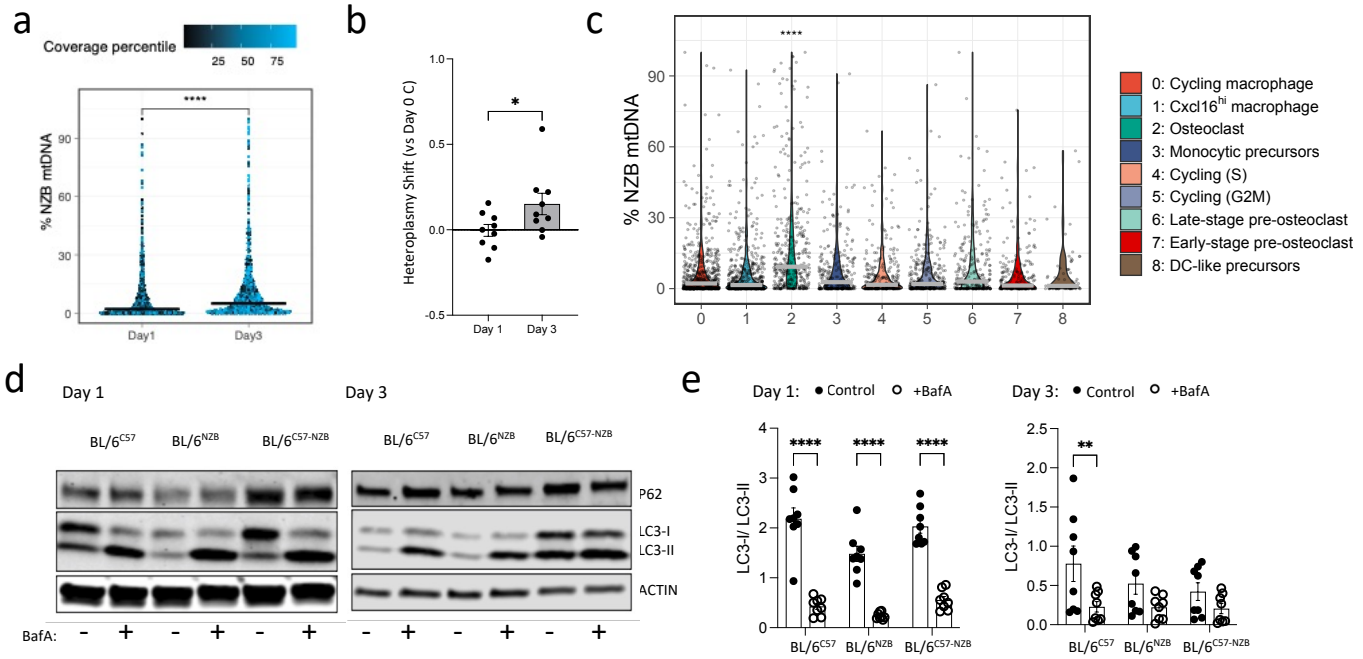
a
Coverage percentile
25 50 75
****
% NZB mtDNA
90
60
30
0
Day1
Day3
b
Heteroplasmy Shift (vs Day 0 C)
1.0
0.5
0.0
-0.5
*
Day 1
Day 3
c
****
% NZB mtDNA
90
60
30
0
0 1 2 3 4 5 6 7 8
0: Cycling macrophage
1: Cxcl16hi macrophage
2: Osteoclast
3: Monocytic precursors
4: Cycling (S)
5: Cycling (G2M)
6: Late-stage pre-osteoclast
7: Early-stage pre-osteoclast
8: DC-like precursors
d
Day 1
Day 3
BL/6C57
BL/6NZB
BL/6C57-NZB
P62
LC3-I
LC3-II
ACTIN
BafA: - + - + - + - + - + - +
e
Day 1: Control +BafA
Day 3: Control +BafA
LC3-I/ LC3-II
****
**
BL/6C57
BL/6NZB
BL/6C57-NZB

Figure 4

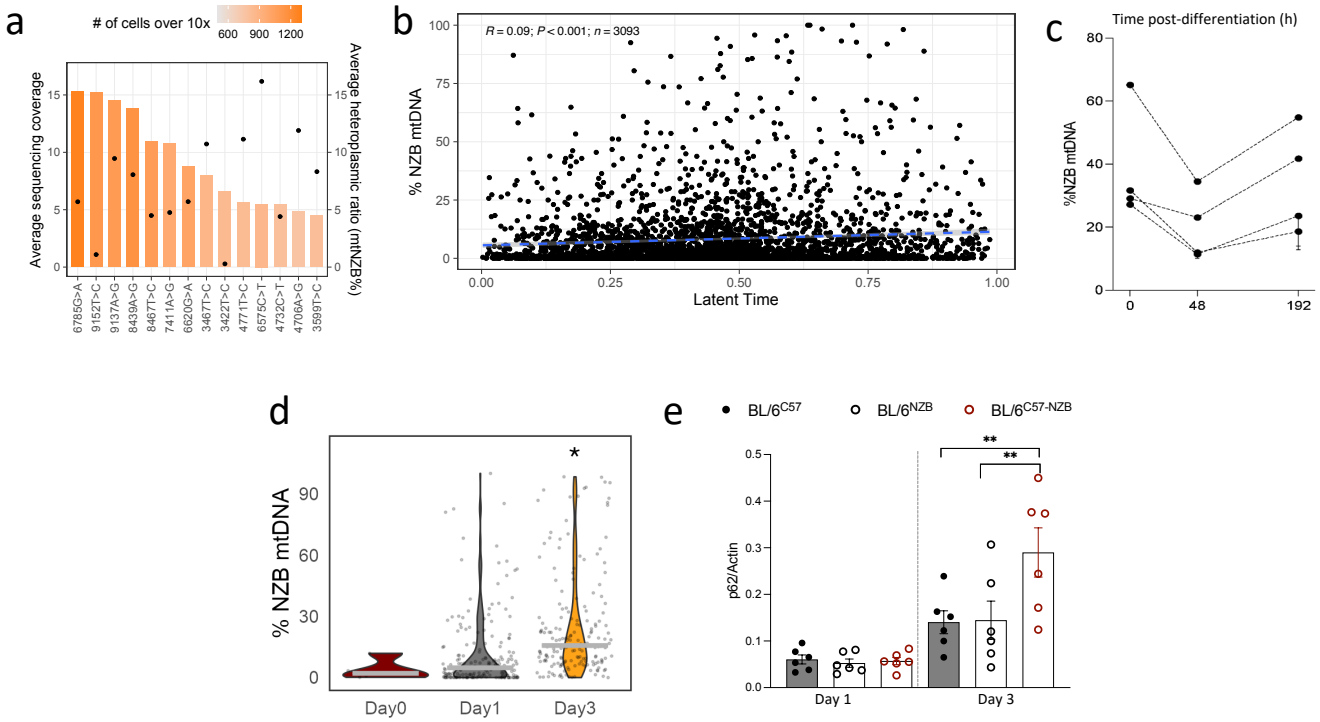

Extended Data Fig. 3

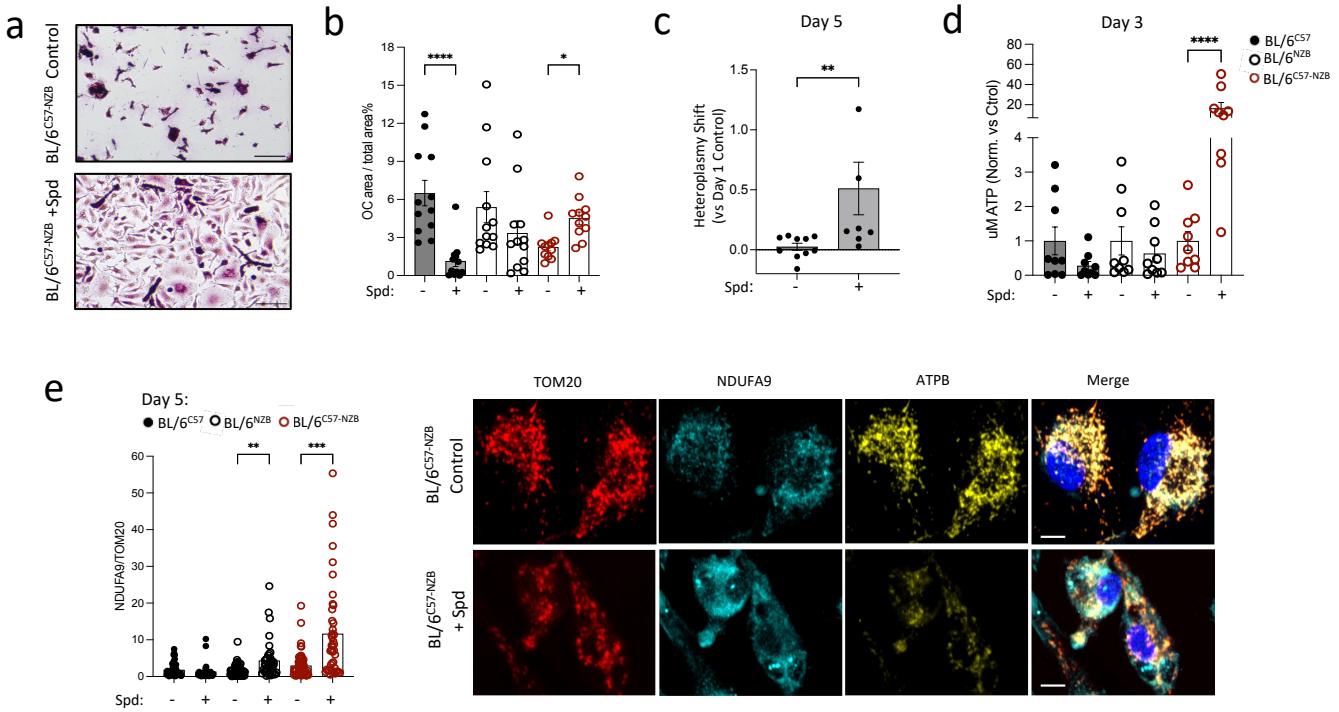
a
BL/6C57-NZB Control
BL/6C57-NZB +Spd
b
OC area / total area%
Spd:
c
Day 5
Heteroplasmy Shift (vs Day 1 Control)
Spd:
d
Day 3
uM ATP (Norm. vs Ctrol)
BL/6C57
BL/6NZB
BL/6C57-NZB
Spd:
e
Day 5:
BL/6C57
BL/6NZB
BL/6C57-NZB
NDUFA9/TOM20
Spd:
TOM20
NDUFA9
ATPB
Merge
BL/6C57-NZB Control
BL/6C57-NZB + Spd

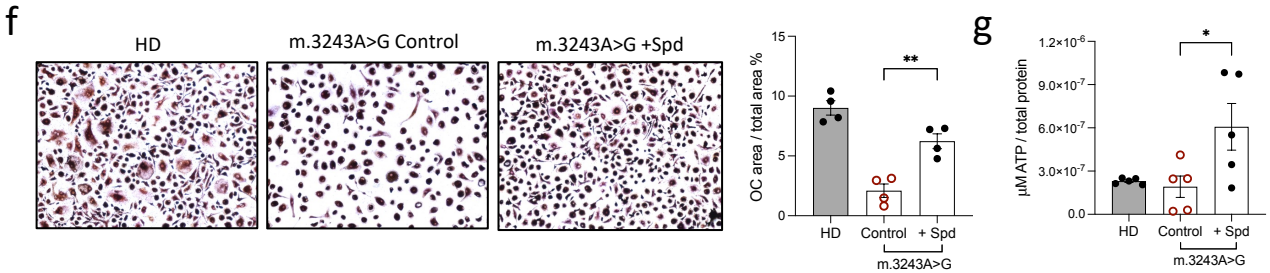
f
HD
m.3243A>G Control
m.3243A>G +Spd
OC area / total area %
HD
Control
+ Spd
m.3243A>G
g
µM ATP / total protein
HD
Control
+ Spd
m.3243A>G

Figure 5

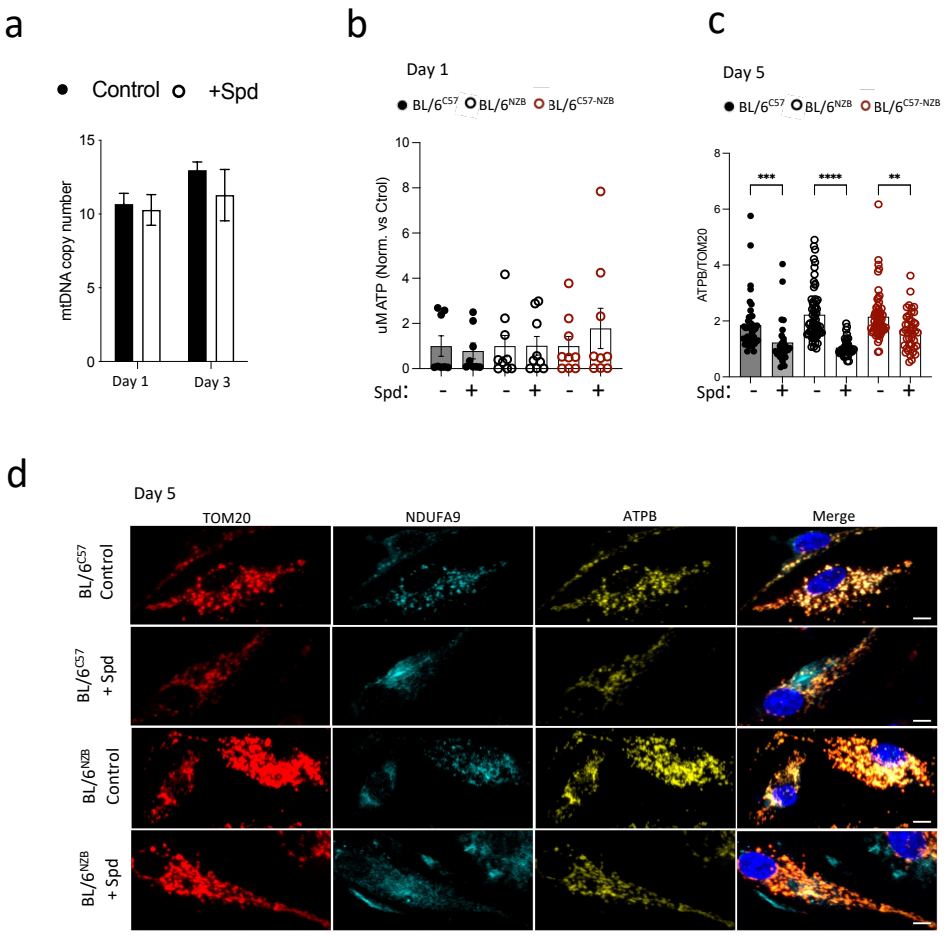

Extended Data Fig. 4

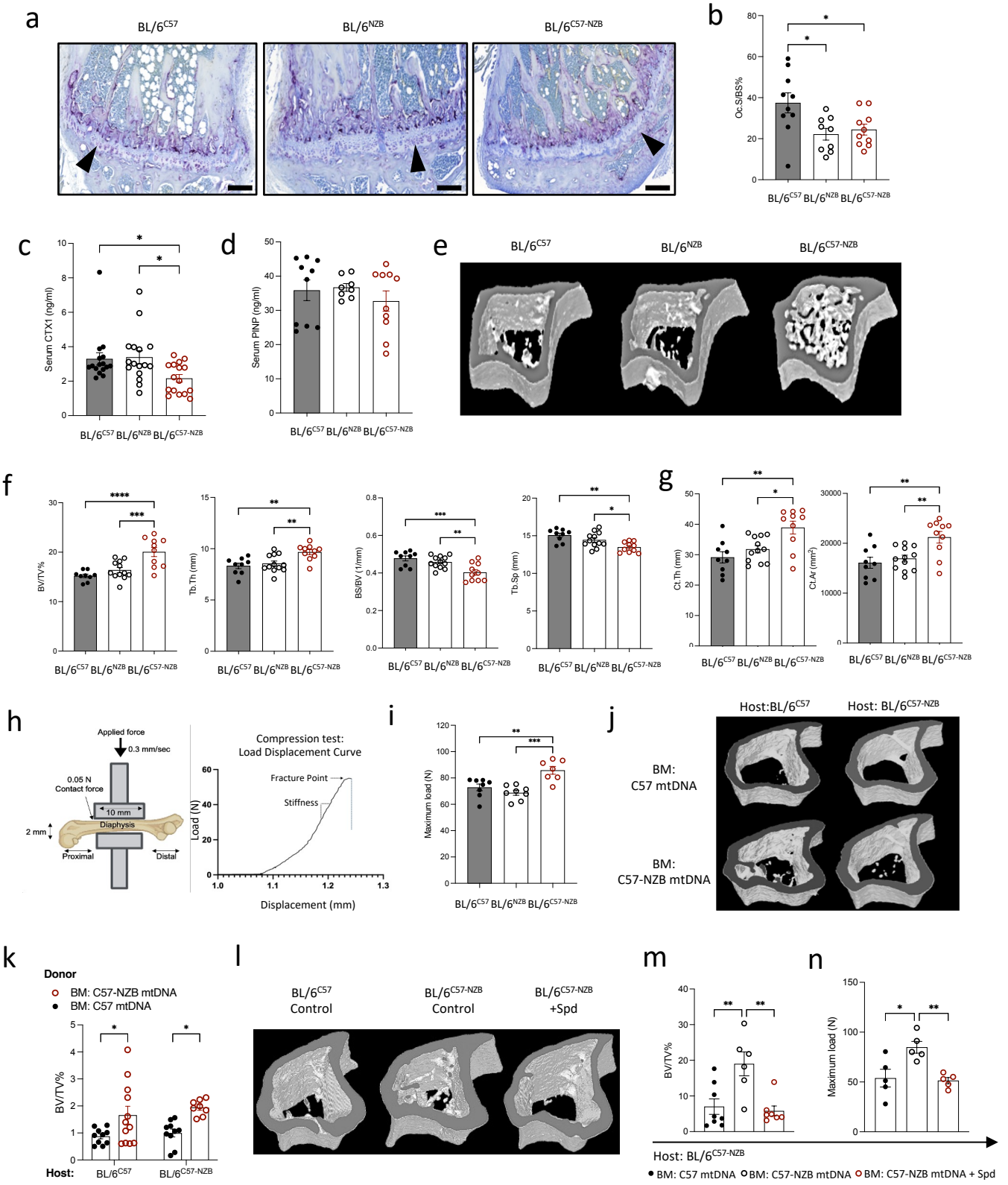
a
BL/6C57
BL/6NZB
BL/6C57-NZB
b
Oc.S/BS%
BL/6C57 BL/6NZB BL/6C57-NZB
c
Serum CTX1 (ng/ml)
BL/6C57 BL/6NZB BL/6C57-NZB
d
Serum PINP (ng/ml)
BL/6C57 BL/6NZB BL/6C57-NZB
e
BL/6C57
BL/6NZB
BL/6C57-NZB
f
BV/TV%
Tb.Th (mm)
BS/BV (1/mm)
Tb.Sp (mm)
BL/6C57 BL/6NZB BL/6C57-NZB
g
Ct.Th (mm)
Ct.Ar (mm2)
BL/6C57 BL/6NZB BL/6C57-NZB
h
Applied force
0.3 mm/sec
0.05 N
Contact force
10 mm
Diaphysis
2 mm
Proximal
Distal
Compression test:
Load Displacement Curve
Fracture Point
Stiffness
Load (N)
Displacement (mm)
i
Maximum load (N)
BL/6C57 BL/6NZB BL/6C57-NZB
j
Host:BL/6C57
Host: BL/6C57-NZB
BM:
C57 mtDNA
BM:
C57-NZB mtDNA
k
Donor
BM: C57-NZB mtDNA
BM: C57 mtDNA
BV/TV%
Host:
BL/6C57
BL/6C57-NZB
l
BL/6C57
Control
BL/6C57-NZB
Control
BL/6C57-NZB
+Spd
m
BV/TV%
n
Maximum load (N)
Host: BL/6C57-NZB
BM: C57 mtDNA
BM: C57-NZB mtDNA
BM: C57-NZB mtDNA + Spd

Figure 6

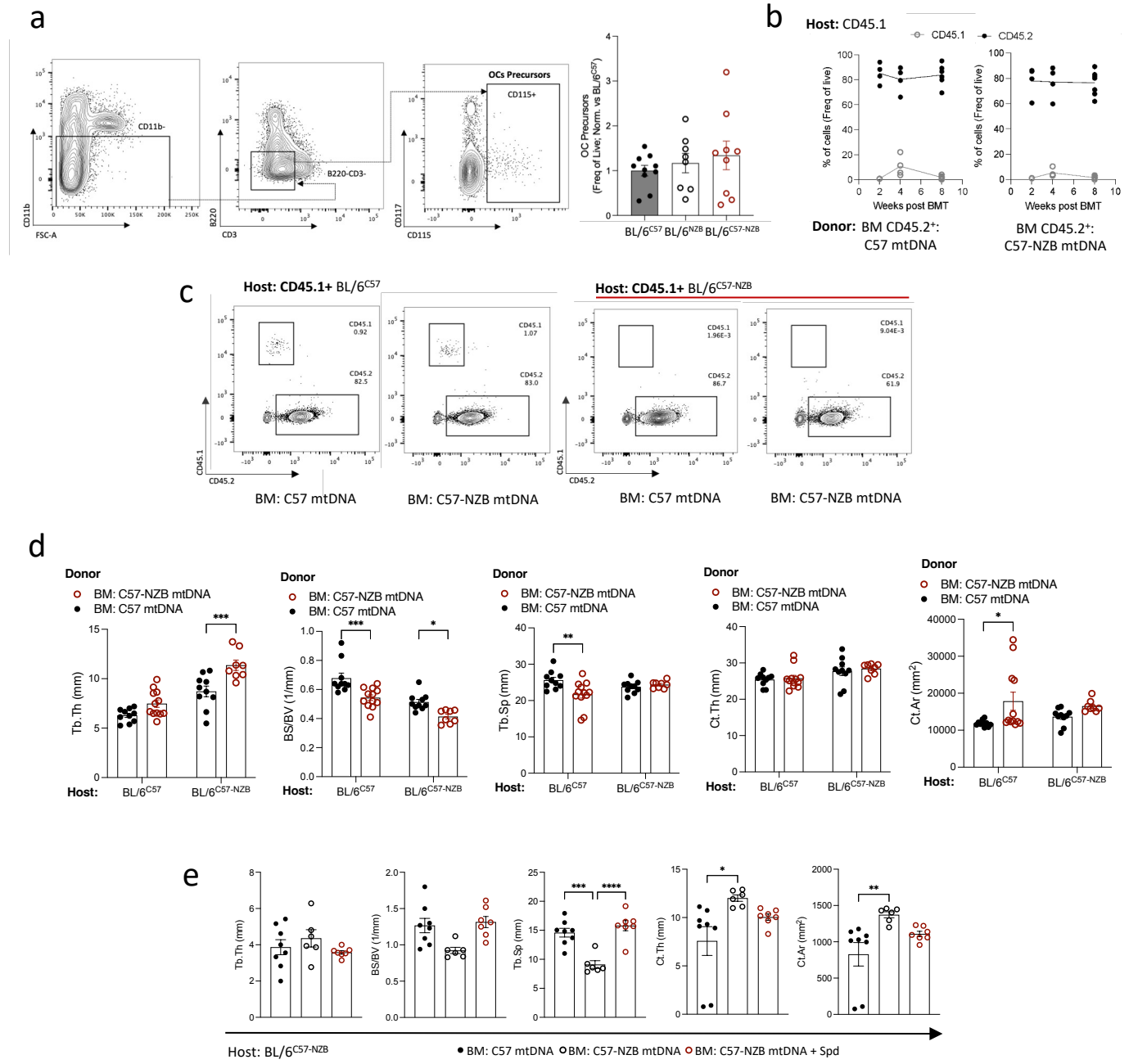

Extended Data Fig. 5

bioRxiv preprint doi: https://doi.org/10.1101/2025.05.02.651799; this version posted August 2, 2025. The copyright holder for this preprint (which was not certified by peer review) is the author/funder. All rights reserved. No reuse allowed without permission.

Supplementary Table 1: NZB mtDNA SNPs identified from scRNA-seq data.

	POS	REF	ALT	GENOTYPE	ID
1	55	G	A	NZB	55G>A
2	716	A	G	NZB	716A>G
3	1353	A	G	NZB	1353A>G
4	1519	G	A	NZB	1519G>A
5	1590	G	A	NZB	1590G>A
6	1822	T	C	NZB	1822T>C
7	2201	T	C	NZB	2201T>C
8	2340	G	A	NZB	2340G>A
9	2525	C	T	NZB	2525C>T
10	2766	A	G	NZB	2766A>G
11	2767	T	C	NZB	2767T>C
12	2798	C	T	NZB	2798C>T
13	2814	T	C	NZB	2814T>C
14	2840	C	T	NZB	2840C>T
15	2934	C	T	NZB	2934C>T
16	3194	T	C	NZB	3194T>C
17	3260	A	G	NZB	3260A>G
18	3422	T	C	NZB	3422T>C
19	3467	T	C	NZB	3467T>C
20	3599	T	C	NZB	3599T>C
21	3692	A	G	NZB	3692A>G
22	3932	G	A	NZB	3932G>A
23	4123	C	T	NZB	4123C>T
24	4276	G	A	NZB	4276G>A
25	4324	T	C	NZB	4324T>C
26	4408	G	A	NZB	4408G>A
27	4706	A	G	NZB	4706A>G
28	4732	C	T	NZB	4732C>T
29	4771	T	C	NZB	4771T>C
30	4885	A	C	NZB	4885A>C
31	4903	T	G	NZB	4903T>G
32	5463	G	A	NZB	5463G>A
33	5552	T	C	NZB	5552T>C
34	5930	G	A	NZB	5930G>A
35	6041	T	C	NZB	6041T>C
36	6407	C	T	NZB	6407C>T
37	6470	A	G	NZB	6470A>G
38	6575	C	T	NZB	6575C>T
39	6620	G	A	NZB	6620G>A
40	6785	G	A	NZB	6785G>A
41	7411	A	G	NZB	7411A>G

bioRxiv preprint doi: https://doi.org/10.1101/2025.05.02.651799; this version posted August 2, 2025. The copyright holder for this preprint (which was not certified by peer review) is the author/funder. All rights reserved. No reuse allowed without permission.

42	7870	G	A	NZB	7870G>A
43	8439	A	G	NZB	8439A>G
44	8467	T	C	NZB	8467T>C
45	8568	C	T	NZB	8568C>T
46	8858	T	C	NZB	8858T>C
47	8864	C	T	NZB	8864C>T
48	9137	A	G	NZB	9137A>G
49	9152	T	C	NZB	9152T>C
50	9391	A	G	NZB	9391A>G
51	9461	T	C	NZB	9461T>C
52	9530	C	T	NZB	9530C>T
53	9581	C	T	NZB	9581C>T
54	9599	A	G	NZB	9599A>G
55	9821	A	T	NZB	9821A>T
56	9985	G	A	NZB	9985G>A
57	10547	C	T	NZB	10547C>T
58	10583	A	G	NZB	10583A>G
59	10952	C	A	NZB	10952C>A
60	11843	G	A	NZB	11843G>A
61	11846	C	T	NZB	11846C>T
62	11933	A	C	NZB	11933A>C
63	12353	C	T	NZB	12353C>T
64	12575	T	A	NZB	12575T>A
65	12695	A	G	NZB	12695A>G
66	12835	T	C	NZB	12835T>C
67	12890	A	G	NZB	12890A>G
68	13004	G	A	NZB	13004G>A
69	13444	C	T	NZB	13444C>T
70	13612	T	C	NZB	13612T>C
71	13689	C	T	NZB	13689C>T
72	13781	A	G	NZB	13781A>G
73	13782	T	C	NZB	13782T>C
74	13837	A	G	NZB	13837A>G
75	13983	A	G	NZB	13983A>G
76	14186	T	C	NZB	14186T>C
77	14211	G	A	NZB	14211G>A
78	14363	A	G	NZB	14363A>G
79	14642	G	A	NZB	14642G>A
80	14738	C	T	NZB	14738C>T
81	15499	T	A	NZB	15499T>A
82	15549	C	T	NZB	15549C>T
83	15578	A	T	NZB	15578A>T
84	15588	C	T	NZB	15588C>T

bioRxiv preprint doi: https://doi.org/10.1101/2025.05.02.651799; this version posted August 2, 2025. The copyright holder for this preprint (which was not certified by peer review) is the author/funder. All rights reserved. No reuse allowed without permission.

85	15603	C	T	NZB	15603C>T
86	15657	T	C	NZB	15657T>C
87	15917	C	T	NZB	15917C>T
88	16017	A	C	NZB	16017A>C
89	16268	A	G	NZB	16268A>G
90	16272	T	C	NZB	16272T>C

Supplementary Table 1: The per-cell heteroplasmic ratio was calculated by dividing the summed allelic coverage of all variants specific to NZB mitochondria (n=90) over the total sequencing coverage at these locations.

bioRxiv preprint doi: https://doi.org/10.1101/2025.05.02.651799; this version posted August 2, 2025. The copyright holder for this preprint (which was not certified by peer review) is the author/funder. All rights reserved. No reuse allowed without permission.

Supplementary Table 2: Algorithms used for bone reconstruction, keep ranked volume, Serial Dilate & Erode, Count Area & Ratio.

Algorithm 1: Bone Reconstruction

Input: $X \in R^{d\times h\times w}$, $x_{bone}, x_{cortical}, n_{frag} \in R$

Output: $V \in \{0,1\}^{d\times h\times w}$

1 Rotate and translate input volume to a standard position and orientation;

2 Extract the whole bone and cortical bones by thresholding: $V^0 \leftarrow nonzero(X - x_{bone})$, $V^1 \leftarrow nonzero(X - x_{cortical})$; /* 'nonzero' is a MATLAB function */

3 Remove the small fragments from the cortical bones' volume: $V^1 \leftarrow bwareaopen(V^1, n_{frag})$;

4 Remove the fibular bone (the second largest volume): $V^0 \leftarrow KeepRankedVol(V^0, -2), V^1 \leftarrow KeepRankedVolume(V^1, 1)$;

5 Dilate and erode the cortical bone to fill the hole inside: $V^1 \leftarrow SerialDilateErode(V^1, [12, -12])$;

6 Intersect the two volumes: $V \leftarrow V^0 \cap V^1$;

7 Return V.

Algorithm 2: Keep Ranked Volume

Input: $V^i \in \{0,1\}^{d\times h\times w}$, $k \in Z$

Output: $V^o \in \{0,1\}^{d\times h\times w}$

1 Find and count the connected components: $V^{cc} \leftarrow bwconncomp(V^i, 26)$; /* 'bwconncomp' is a MATLAB function */

2 Creates a label matrix corresponding to each connected component: $L^{cc} \leftarrow labelmatrix(V^{cc})$; /* 'labelmatrix' is a MATLAB function */

3 Calculate parameters of each component: $AreaProp \leftarrow regionprops(V^{cc}, 'Area')$; /* 'regionprops' is a MATLAB function */

Sort the areas: $(\cdot, index_{sort}) \leftarrow sort(AreaProp, 'descend')$;

4 Copy the volume: $V^o \leftarrow V^i$;

5 If $k > 0$ do:

6 Remove the components other than the kth largest volume: $V^o[L^{cc}! = k] \leftarrow 0$;

7 Else do:

8 Remove the components of the kth largest volume: $V^o[L^{cc} == k] \leftarrow 0$;

9 End

10 Return V^o.

11

bioRxiv preprint doi: https://doi.org/10.1101/2025.05.02.651799; this version posted August 2, 2025. The copyright holder for this preprint (which was not certified by peer review) is the author/funder. All rights reserved. No reuse allowed without permission.

Algorithm 3: Serial Dilate & Erode

Input: $V^i \in \{0,1\}^{d\times h\times w}$, $[t_1 \cdots t_k] \in Z^k$

Output: $V^o \in \{0,1\}^{d\times h\times w}$

Set the parameter size of structure element: $size$;

Initialize a structure element: $se \leftarrow strel('cube', size)$; /* 'strel' is a MATLAB */

Initialize the volume: $V^o \leftarrow V^i$;

Foreach $i \in [1, k] \cap Z$ do:

  Foreach $j \in [1, abs(t_i)] \cap Z$ do:

    If $t_i > 0$ do:

    Dilate the volume to fill the hole inside: $V^o \leftarrow imdilate(V^o, se)$;

      Elseif $t_i < 0$ do:

        Erode the volume to fit a specific size: $V^o \leftarrow imerode(V^o, se)$;

  End

End

Return V^o.

Algorithm 4: Count Area & Ratio

Input: $I^i \in R^{h\times w}$, $\tau \in R$, $n_{conn} \in Z$, $M^i \in \{0,1\}^{h\times w}$

Output: $M^r \in \{0,1\}^{h\times w}$, $a^r \in R^m$, $r^r \in R^m$

Normalize the input image: $I^o \leftarrow (I^i - I^i)/(I^i - I^i + 10^{-5})$;

Filter the image using a high passing filter: $I^o \leftarrow (1 - G) * I^i$; /* G is a gaussian filter kernel function */

Get the areas of the red channel: $M^r \leftarrow (I^o[\cdots,1] > \tau[1])\&(I^o[\cdots,2] < \tau[2])\&(I^o[\cdots,3] < \tau[3])$;

Find and count the connected components: $M^{cc} \leftarrow bwconncomp(M^i, 8)$; /* 'bwconncomp' is a MATLAB function */

Creates a label matrix corresponding to each connected component: $L^{cc} \leftarrow labelmatrix(M^{cc})$; /* 'labelmatrix' is a MATLAB function */

Calculate parameters of each component: $AreaProp \leftarrow regionprops(M^{cc}, 'Area')$; /* 'regionprops' is a MATLAB function */

Get the number of components: $m \leftarrow |AreaProp| - 1$;

Initialize the areas and ratios for each component: $a^r \leftarrow [0]_{m\times 1}$, $r^r \leftarrow [0]_{m\times 1}$

bioRxiv preprint doi: https://doi.org/10.1101/2025.05.02.651799; this version posted August 2, 2025. The copyright holder for this preprint (which was not certified by peer review) is the author/funder. All rights reserved. No reuse allowed without permission.

Foreach $i \in [1, m] \cap Z$ do:

  $a^r[i] \leftarrow \sum(L^{cc} == i + 1) \cap M^r$;

  $r^r[i] \leftarrow a^r[i] / \sum(L^{cc} == i + 1)$;

End

Return M^r, a^r, r^r.